PAPER • OPEN ACCESS

Overview of the recent experimental research on the J-TEXT tokamak

To cite this article: Yonghua Ding *et al* 2024 *Nucl. Fusion* **64** 112005

OPEN ACCESS
IOP Publishing | International Atomic Energy Agency
Nuclear Fusion
Nucl. Fusion **64** (2024) 112005 (19pp)
https://doi.org/10.1088/1741-4326/ad336e

Overview of the recent experimental research on the J-TEXT tokamak

Yonghua Ding[1], Nengchao Wang[1,*], Zhongyong Chen[1], Donghui Xia[1], Zhoujun Yang[1], Zhipeng Chen[1], Wei Zheng[1], Wei Yan[1], Da Li[1,2], Song Zhou[1], Xin Xu[1], Xiaoyi Zhang[1], Feiyue Mao[1], Jiangang Fang[1], Zhengkang Ren[1], Xixuan Chen[1], Junli Zhang[1], Xiaobo Zhang[1], Ying He[1], Qi Zhang[1], You Li[1], Wei Bai[1], Lingke Mou[1], Feng Li[1], Ting Long[2], Rui Ke[2], Li Gao[1], Peng Shi[3], Chengshuo Shen[1], Jiaxing Liu[1], Weixin Guo[1], Lu Wang[1], Hanhui Li[1,4], Zhonghe Jiang[1], Xiaoqing Zhang[1], Jianchao Li[5], Bo Rao[1], Zhifeng Cheng[6], Ping Zhu[1], Minghai Liu[1], Tao Xu[1], Shaoxiang Ma[1], Yong Yang[1], Chuan Li[1], Zhijiang Wang[1], Ming Zhang[1], Kexun Yu[1], Xiwei Hu[1], Y. Liang[1,3,7], Q. Yu[8], K. W. Gentle[9], Yuan Pan[1] and the J-TEXT Team: Yonghua Ding[1], Yuan Pan[1], Kenneth William Gentle[10], Xiwei Hu[1], Kexun Yu[1], Qingquan Yu[8], Yunfeng Liang[1,7,3], Donghui Xia[1], Ming Zhang[1], Li Gao[1], Lu Wang[1], Zhongyong Chen[1], Zhijiang Wang[1], Zhonghe Jiang[1], Zhipeng Chen[1], Zhoujun Yang[1], Zhifeng Cheng[6], Xiaoqing Zhang[1], Minghai Liu[1], Tao Xu[1], Ping Zhu[1], Wei Jiang[11], Lin Yi[11], Ya Zhang[12], Bo Rao[1], Qiming Hu[13], Wei Zheng[1], Shaoxiang Ma[1], Yong Yang[1], Chuan Li[1], Nengchao Wang[1], Jianchao Li[14], Mingxiang Huang[15], Weixin Guo[1], Wei Yan[1], Da Li[2,1], Haolong Li[16], Zhuo Huang[15], Song Zhou[1], Jie Huang[1], Hanhui Li[4,1], Weijun Wang[1], Mei He[1], Qing Zhao[1], Jiayu Xu[1], Gangyi Zhou[1], Weigang Ba[1], Cheng Yang[1], Junjie Yao[1], Chuliang Wang[1], Bo He[1], Yongzhen Hu[1], Mingyang Deng[1], Jingwei Fu[1], Meiling Liang[1], Yehong Guan[1], Hongyan Wu[1], Ge Zhuang[17], Weixing Ding[17], Tao Lan[17], Shiyong Zeng[17], Malik Sadam Hussain[17,1], Peng Shi[3], Zhifang Lin[18], Hai Liu[19], Youwen Sun[3], Long Zeng[3], Shaocheng Liu[3], Liang Liao[3], Wulyu Zhong[2], Zhongbing Shi[2], Min Jiang[2], Yunbo Dong[2], Min Xu[2], Aike Wang[2], Xiaolong Zhang[2], Linzi Liu[2], Ruihai Tong[2], Jun Cheng[2], Lin Nie[2], Rui Ke[2], Ting Long[2], Hui Li[2], Jianqiang Xu[2], Zengchen Yang[2], Jie Wen[2], Anshu Liang[2], Yipo Zhang[2], Yifan Wu[2], Chengyuan Chen[2], Kaijun Zhao[20], Yuejiang Shi[21], He Huang[10], Max Austin[10], Sanggon Lee[22], Neville C. LuhmannJr[23], Calvin W. Domier[23], Yilun Zhu[23], David L. Brower[24], Jie Chen[24], K. Ida[25], Y. Takemura[25], Y. Suzuki[26], K. Nagasaki[27], P. Drews[7], A. Knieps[7], Xiang Han[7], A. Krämer-Flecken[7], M. Henkel[7], Jiyang He[1], Yinan Zhou[1], Ruo Jia[1], Ying He[1], Yue Peng[1], Qi Zhang[1], Pengyu Wang[1], Xin Xu[1], Jiawei Li[1], You Li[1], Feiyue Mao[1], Xiaoyi Zhang[1], Jie Yang[1], Conghui Lu[1], Junli Zhang[1], Yiwei Lu[1], Rumeng Wang[1], Hongqi Zhang[1], Yingqin Zeng[1], Chengshuo Shen[1], Jiangang Fang[1], Zhengkang Ren[1], Guodong Zhang[1], Xixuan Chen[1], Fangyuan Ma[1], Abba Alhaji Bala[1], Dingchen Li[1], Jiankun Hua[1], Xinkun Ai[1], Qinlin Tao[1], Yu Zhong[1], Yangbo Li[1], Xiangrui He[1], Sui Wan[1], Shanni Huang[1], Yiming Ma[1], Zitong Qu[1], Shimin Yu[1], Zhangsheng Huang[1], Chi Lei[1], Qinghu Yang[1], Jiaxing Liu[1], Fengming Xue[1], Chuanxu Zhao[1], Junhui Yang[1], Zili Chen[1], Jingmin Yang[1], Shengyang Xiao[1], Shiwei Xue[1], Wentao Geng[1], Jian Zhang[1], Xiong Tao[1], Zhigang Hao[1], Qiong Li[1], Jinyu Xiong[1], Huakun Cai[1], Mingzhu Zhang[1], Yaping Zhang[1], Yangming Zhao[1], Qiancheng Zhao[1], Wei Bai[1], Shaodong Jiao[1], Dongliang Han[1], Shiyi Peng[1], Jiaolong Dong[1], Qinglong Yang[1], Fan Gu[1], Zhaosu Wang[1], Hao Wang[1], Shu Yang[1], Yang Zhao[1], Wang Lin[1], Guoyao Fan[1],

[*] Author to whom any correspondence should be addressed.

Kehong Dong[1], Xiehang Ren[1], Feng Li[1], Ce Deng[1], Feng Han[1], Jing Liu[1], Qiqi Wu[1], Fei Xie[1], Yujie Zhong[1], Zinan Wei[1], Wanjun Qing[1], Chu Han[1], Hui Ye[1], Xiaobo Zhang[1], Yingzhou Jiang[1], Lingke Mou[1], Chengyu Yang[1], Shuhao Li[1], Jianjun Yuan[1], Haojie Chen[1], Xiaobo Liu[1], Wentong Shang[1], Shengyuan Guan[1], Chouyao Tang[1], Sheng Li[1], Jiamao Gao[1], Wenting Weng[1], Shouqi Xiong[1], Yuan Gao[1], Zhichao Zhang[1], Boliang Zhu[1], Fuyou He[1], Feiyang Wu[1], Xianqian Zha[1], Tong Guo[1], Xiaohan Xie[1], Ruiyang Xu[1], Weikang Zhang[1], Zixiao Jiao[1], Chupin Fu[1], Chengzhi Guo[1], Sifen He[1], Yixing Jiang[1], Xianghao Kong[1], Cunkai Li[1], Feng Li[1], Zhen Li[1], Renzhe Liu[1], Ye Tian[1], Wenshan Wang[1], Yuhan Wang[1], Zutao Wang[1], Dengfeng Xu[1], Wendi Yang[1], Bangyou Zhu[1], Guangding Zhu[1], Xiating Mou[1], Xianlong Liu[1], Ziyang Jin[1], Jiaming Wang[1], Xinyu Cao[1], Yifan Wu[1], Cheng Han[1], Yanqiu Chen[1], Fanxi Liu[1], Haiqing Wang[1], Wei Xie[1], Wen Wang[1], Yutong Yang[1], Shaoyu Wang[1], An Mao[1], Peilong Zhang[1], Yanhao Zhao[1], Hengbun Ma[1], Zhiheng Li[1], Keze Li[1], Qiang Luo[1], Yuting Huang[1], Menghan Xiao[1], Yifei Huang[1], Guinan Zou[1], Yajun Wang[1], Dunrui Zhang[1], Zhi Zhang[1], Chaoxiang Guo[1], Bo Hu[1], Dengkuo Zhang[1], Junang Zhang[1], Jinlong Guo[1], Nan Wang[1], Qixiong Fu[1], Yisong Zhang[1], Jiong Guo[1], Yinlong Yu[1], Weijie Lin[1], Liye Wang[1], Jingtao Li[1], Zhangrong Hou[1], Xiaopeng Yi[1], Yi Zhang[1], Runyu Luo[1], Zijian Xuan[1], Xiping Jiang[1], Zisen Nie[1], Zhiyu Meng[1], Ziying Jiang[1], Xinyu Fang[1], Yuxuan Huang[1], Ning Peng[1], Xinyi Jin[1], Yujun Zhang[1], Zhongkai Li[1], Yuchen Zhang[1], Weimin Fu[1], Zijuan Dong[1], Yuhuan Liu[1], Anqi Hu[1], Zekai Guo[1], Weijie Ye[1], Zhenchang Du[1], Xun Zhou[1], Zhiyu Tang[1], Yan Guo[1], Zhiwen Yang[1], Xinchen Yao[1], Zezhi Yu[1], Boyu Zhao[1], Ruomu Wang[1], Yuwei Sun[1], Haocheng Wang[1], Tianyu Zheng[1], Chaofan Lu[1], Tianjing Wang[1], Zhuolong Li[1], Xiangyu Fu[1], Yulong Deng[1], Haojun Yu[1], Yuan Sheng[1], Yuanji Sun[1], Zi'an Mao[1], Lei Yu[1], Shaohua Ye[1], Wenjie Zhang[1], Qihang Jiang[1], Yushen Zhou[1], Jianfeng Zhu[1], Kexu Liu[1], Jinqiang Mao[1], Yunxiao Han[1], Zhihao Mai[1], Huchuan Zou[1], Jianliang Zheng[1] and Zhiqiang Liu[1]

[1] State Key Laboratory of Advanced Electromagnetic Technology, International Joint Research Laboratory of Magnetic Confinement Fusion and Plasma Physics (IFPP), School of Electric and Electronic Engineering, Huazhong University of Science and Technology, Wuhan 430074, China
[2] Southwestern Institute of Physics, Chengdu, China
[3] Institute of Plasma Physics, Chinese Academy of Sciences, Hefei, China
[4] Guizhou University of Commerce, Guiyang, China
[5] Wuhan Institute of Technology, Wuhan, China
[6] ITER Organization, Route de Vinon-sur-Verdon, CS 90 046, 13067 St. Paul Lez Durance Cedex, France
[7] Forschungszentrum Jülich GmbH, IEK-Plasmaphysik, Jülich, Germany
[8] Max-Planck-Institut für Plasmaphysik, Garching, Germany
[9] Institute of Fusion Studies, University of Texas at Austin, Austin, TX, United States of America
[10] University of Texas at Austin, Austin, TX 78712, United States of America
[11] School of Physics, Huazhong University of Science and Technology, Wuhan 430074, China
[12] Department of Physics, Wuhan University of Technology, Wuhan 430070, China
[13] Princeton Plasma Physics Laboratory, PO Box 451, Princeton, NJ 08543, United States of America
[14] Hubei Key Laboratory of Optical Information and Pattern Recognition, Wuhan Institute of Technology, Wuhan, 430205, China
[15] College of Computer Science, South-Central University for Nationalities, Wuhan 430074, China
[16] Shenzhen University, Shenzhen 518060, China
[17] University of Science and Technology of China, Hefei 230026, China
[18] School of Electrical Engineering & Automation, Jiangsu Normal University, Xuzhou 221116, China
[19] Southwest Jiaotong University, Chengdu, China
[20] College of Nuclear Science and Engineer, East China University of Technology, PO Box 330013, Nanchang, China
[21] ENN Science and Technology Development Co., Ltd, & Hebei Key Laboratory of Compact Fusion, Langfang 065001, China
[22] National Fusion Research Institute, Daejeon 305-333, Korea, Republic Of
[23] University of California, Davis, CA 95616, United States of America
[24] University of California Los Angeles, Los Angeles, CA 90095, United States of America
[25] National Institute for Fusion Science, 509-5292 Toki, Japan
[26] Graduate School of Advanced Science and Engineering, Hiroshima University, Higashi-Hiroshima 739-8527, Japan
[27] Institute of Advanced Energy, Kyoto University, Gokasho, Uji, Kyoto 611-0011, Japan

E-mail: wangnc@hust.edu.cn and yhding@hust.edu.cn

Received 27 November 2023, revised 2 February 2024
Accepted for publication 13 March 2024
Published 19 August 2024

Abstract

The J-TEXT capability is enhanced compared to two years ago with several upgrades of its diagnostics and the increase of electron cyclotron resonance heating (ECRH) power to 1 MW. With the application of electron cyclotron wave (ECW), the ECW assisted plasma startup is achieved; the tearing mode is suppressed; the toroidal injection of 300 kW ECW drives around 24 kA current; fast electrons are generated with toroidal injected ECW and the runaway current conversion efficiency increases with ECRH power. The mode coupling between 2/1 and 3/1 modes are extensively studied. The coupled 2/1 and 3/1 modes usually lead to major disruption. Their coupling can be either suppressed or avoided by external resonant magnetic perturbation fields and hence avoids the major disruption. It is also found that the 2/1 threshold of external field is significantly reduced by a pre-excited 3/1 mode, which can be either a locked island or an external kink mode. The disruption control is studied by developing prediction methods capable of cross tokamak application and by new mitigation methods, such as the biased electrode or electromagnetic pellet injector. The high-density operation and related disruptions are studied from various aspects. Approaching the density limit, the collapse of the edge shear layer is observed and such collapse can be prevented by applying edge biasing, leading to an increased density limit. The density limit is also observed to increase, if the plasma is operated in the poloidal divertor configuration or the plasma purity is increased by increasing the pre-filled gas pressure or ECRH power during the start-up phase.

Keywords: J-TEXT tokamak, ECRH, resonant magnetic perturbation, disruption control, density limit, turbulence

(Some figures may appear in colour only in the online journal)

1. Introduction

As of a long-term research program, the J-TEXT [1–3] experiments aim to develop fundamental physics and control mechanisms of high temperature tokamak plasma confinement and stability in support of the successful operation of ITER and the design of future Chinese fusion reactor, CFETR. In this paper, the J-TEXT results achieved over the last two years, especially on the electron cyclotron resonance heating (ECRH) physics, magnetohydrodynamics (MHD) instabilities, plasma disruptions, turbulence and transport, will be presented. These physical achievements are obtained under the supports of diagnostics and ECRH systems, and they will be introduced as follows.

1.1. Development of diagnostics

Several diagnostics are upgraded or newly developed on J-TEXT. To simultaneously measure the electrostatic and magnetic fluctuations in the plasma boundary, a combined Langmuir-magnetic probe is developed [4], and it consists of 8 graphite probe pins and a set of magnetic probes measuring three directions. An improved design of cutting the graphite sleeve helps the probe to reduce the shielding effect of eddy current for exploring the magnetic fluctuation. A new heterodyne collective scattering system based on a dual-HCN laser (337 μm) is designed and developed for investigating the turbulence transport in the core region. This system includes 3 channels with different detection angles for measuring density fluctuations with $2 \leqslant k_{\perp} \leqslant 12\ \mathrm{cm}^{-1}$ [5]. A gas puffing imaging (GPI) diagnostic is newly developed for measuring the two-dimensional turbulence in the edge region. The GPI covers the area 10 cm $\times$ 10 cm cross the last closed flux surface (LCFS), and can provide 100 000 frames per second with 256 $\times$ 256 pixels [6]. The phase resolution of a Faraday rotation angle of the J-TEXT three-wave polarimeter-interferometer system (POLARIS) is improved from 0.1° to 0.06° [7], which can show the sawtooth oscillations clearly. An upgraded equilibrium reconstruction method is developed by combining the POLARIS data and the equilibrium and fitting code, and the temporal and spatial distribution of electron density and current density can be reconstructed more accurately [7]. A classification algorithm with high classification accuracy rate (reaches 93.8%) based on machine learning is designed and realized to classify J-TEXT electron cyclotron emission imaging (ECEI) signals automatically. In order to improve the quality of the ECEI signal, a feedback conditioning unit is also developed that combines the J-TEXT ECEI digital control function and a classification algorithm [8].

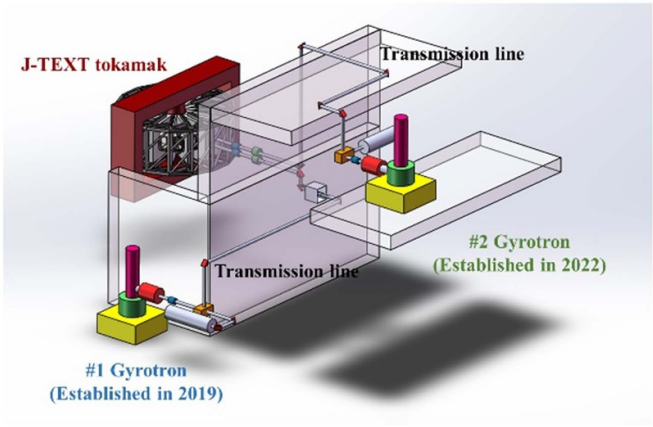

Figure 1. Layout diagram of the J-TEXT ECRH system. Reproduced from [10]. CC BY 4.0.

1.2. Upgrade of the ECRH systems

To increase the plasma parameters and to enhance the capability of controlling the plasma, J-TEXT continuously makes great efforts on upgrading its auxiliary heating systems. Recently, a total ECRH power of 1 MW is available on J-TEXT, with the successful commission of the second gyrotron (105 GHz/500 kW/1 s) in the end of 2022 [9, 10]. On J-TEXT, the 1 MW ECRH system [10] consists of two GYCOM gyrotrons (105 GHz/500 kW/1 s) and they are generally operated at the second harmonic X-mode (X2 mode). The #1 gyrotron was firstly put into physical experiments in 2019. More than 400 kW electron cyclotron wave (ECW) power injection was achieved, increasing the core electron temperature (T_{e0}) from about 0.9 keV to about 1.5 keV [2, 11]. The commissioning of the #2 gyrotron was finished successfully in 2022. The simultaneously injection of ECW from both gyrotrons was achieved in May 2023, increasing T_{e0} to above 2 keV.

Figure 1 shows the layout of the J-TEXT ECRH system. Two transmission lines based on corrugated waveguides are built for the two gyrotrons. An integrated dual-launcher is designed and manufactured. The transmission lines and launcher could transmit ECW and inject it into the plasma with high efficiency. The amount of the transmission loss caused by those components is 7%–12%. Thus, more than 800 kW ECW can be injected into the plasma with 1 MW ECW power generated by the gyrotrons. As for the dual-launcher, the injection angles can vary from $-10°$ to $+15°$ toroidally and from $-15°$ to $+15°$ poloidally [9].

2. Physics study with the injection of ECW

ECW is one of the key tools in ITER for heating and current drive [12], assisting the plasma startup [13], controlling MHD instabilities (e.g. neoclassical tearing mode (NTM), sawtooth, disruption, etc) [14], impurities [15], and so on. The ECW power in ITER is planned to upgrade from 40 MW to 67 MW in DT-1 [16], which promotes ECW to a more essential position. Further researches with the injection of ECW become more important. The above physics problems are investigated

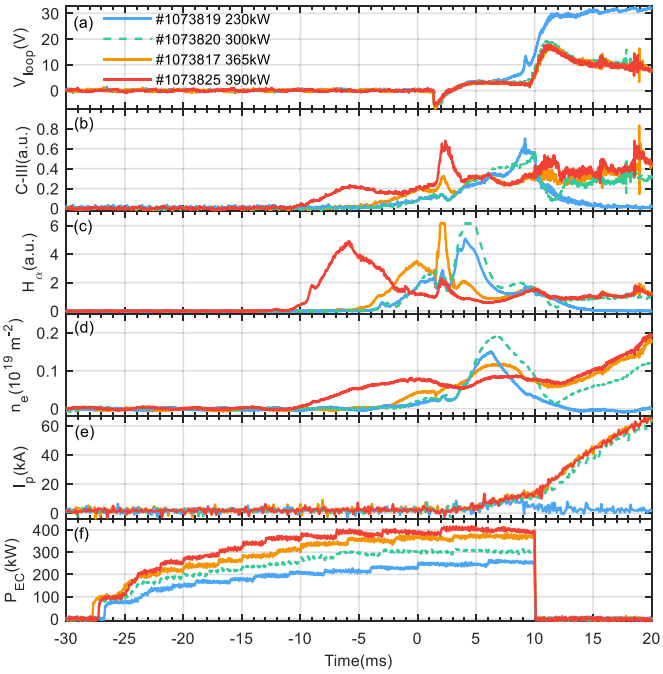

Figure 2. The temporal evolution of plasma parameters during start-up assisted by ECRH: (*a*) loop voltage with $V_{loop} = (2\pi R_0)\ ^* E_\varphi$, (*b*) C-III emission, (*c*) H_α emission, (*d*) the core line-integrated electron density, (*e*) plasma current, (*f*) the injected ECW power. Reproduced from [20]. © 2023 The Author(s). Published on behalf of IAEA by IOP Publishing Ltd.

recently in J-TEXT, and they are summarized in the following subsections.

2.1. Plasma start-up assisted by ECRH

ECW has been widely demonstrated to be an effective tool for assisting the plasma start-up with a low toroidal electric field (E_φ) [17, 18]. Such scenario is essential for a superconducting device, especially ITER [19], while the critical ECW power required for ITER's first plasma remains unclear. To support the ITER research, the plasma start-up assisted by the X2 mode ECW is on J-TEXT [20], so as to determine the minimum ECW power requirement and to develop a better physics description of the process. By injecting the ECW into vacuum vessel before the application of E_φ, the minimum E_φ for successful start-up is reduced from 2.5 V m^{-1} (ohmic) to 0.56 V m^{-1} (ECRH). The critical ECW power for a successful start-up is determined to be approximately 200 kW, while 300 kW ECW can ensure robust breakdown, as illustrated in figure 2. A higher ECRH power effectively induces high H_α emission in a localized region, comparable to the effects of E_φ. A low ECW power of about 150–200 kW can create ionization in J-TEXT, which can be extrapolated to 5.2–7 MW for ITER [20].

2.2. Suppression of TMs by ECRH

With the perpendicular injection of ECW, 2/1 classical tearing modes (TMs) can be completely suppressed if the ECW power

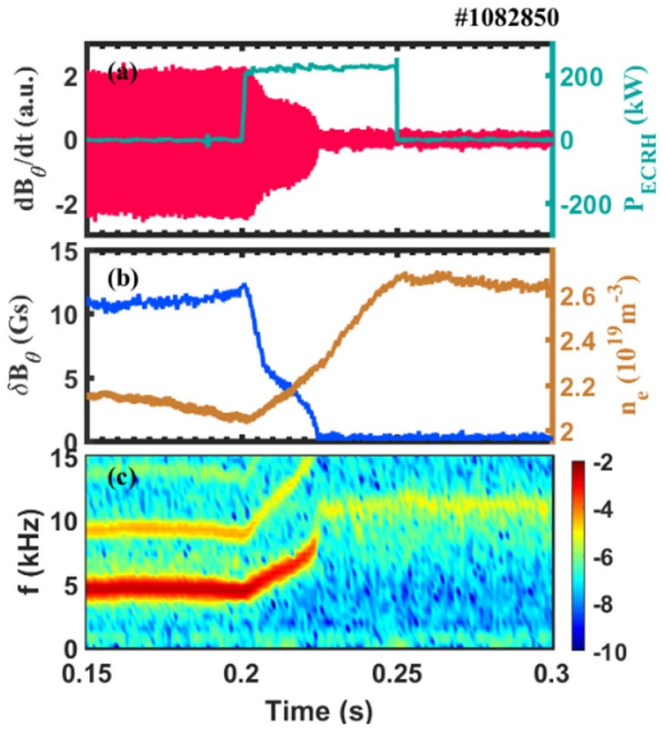

Figure 3. The complete suppression of 2/1 TM by 226 kW ECRH. (*a*) ECW power and Mirnov signal. (*b*) The perturbed poloidal magnetic field (δB_θ) generated by TM and line averaged electron density. (*c*) The spectrum of Mirnov signal.

is deposited close to the rational surface (RS) [21]. Figure 3 displays a typical example of the TM suppression by 226 kW ECRH. Once ECW is turned on, the TM amplitude decreases significantly within 8 ms, as indicated by the perturbed poloidal magnetic perturbation (MP) δB_θ shown in figure 3(*b*). After a fast reduction, the TM amplitude decreases slowly until the mode is completely suppressed at 0.225 s. The core line averaged electron density (n_{e0}) increases by 35% after the mode suppression (figure 3(*b*)). The TM does not reappear even after the removal of ECW. Lower ECW power can only partially suppress the TM, and TM amplitude recovers after the ECW being turned off. The heating effect may play a dominant role on the TM suppression.

2.3. Observations with the toroidal injection of ECW

For toroidal injection, the ECW drives toroidal plasma current, i.e. electron cyclotron current drive (ECCD). Improving ECCD efficiency is of great importance for the stabilization of NTM and the reduction of ECCD power threshold. The investigation of ECCD efficiency is carried out on J-TEXT [22]. The current drive efficiency (η_0) is generally defined by $\eta_0 = I_{rf} n_e R / P_{ECCD}$, where I_{rf} the driven current by ECCD, n_e the electron density, R the major radius and P_{ECCD} the injected power of ECCD. Since the zero-loop voltage operation is not yet achieved on J-TEXT, hence I_{rf} does not equal to I_p. The ECCD efficiency is then estimated by measuring the change in loop voltage between the pure ohmic heating case and the ECCD case, ΔV. And by scanning the ECW power with fixed I_p and n_e, the relative drop in loop voltage ($-\Delta V/V_{OH}$) can be described as a function of the normalized ECW power, $P_{norm} = P_{ECCD}/n_e I_p R$. The non-zero loop voltage can lead to non-zero ohmic current and accelerate the fast electrons increasing the effective current drive efficiency. By taking these two effects into account, this function can be written as $-\Delta V/V_{OH} = (\eta_0 + \eta_1)P_{norm}/(1 + \eta_1 P_{norm})$, and then η_0 can be determined by carrying out a least square fit for the experimental data with this function. Figure 4 displays the results from ECW power scan experiments at different n_e and ECCD toroidal angles. η_0 is estimated in the range of 0.06–0.16 $\times$ 10^{19} A m^{-2} W^{-1}. The total driven current is then estimated to be ~24 kA ($I_p = 100$ kA) with 300 kW ECW. It is noted that T_{e0} increases linearly (e.g. from 0.8 keV to 1.5 keV) with the increase of P_{ECCD} (from 0 to 300 kW) at fixed n_e (at 1.5 $\times$ 10^{19} m^{-3} for the red dots shown in figure 4(*a*)). With the T_{e0} increase, the conductivity is increased, which might lead to larger driven current. Taking this effect into account, the fitting using the modified function gives a similar η_0 as figure 4, and a variation of 79% for η_1, as described in [22] for details. This indicates that the T_e variation is still too small to produce a measurable η_0 change. Figure 4(*a*) indicates that η_0 increases with n_e. This is consistent with the results on DIII-D [23], where the dimensionless current drive efficiency is derived to be proportional to n_e with a relationship of $\xi \approx 3.3 I_{EC} R n_e / P_{EC} T_e$. Figure 4(*b*) exhibits a difference in η_0 for $\Phi = -20°$ and $+20°$. This may be due to that the synergistic interaction between the residual E_φ and the ECCD is different for the cases of co-injection and counter-injection [24].

The fast electron bremsstrahlung (FEB) diagnostic is a highly effective tool for exploring the plasma physics of ECCD. Fast electrons could be generated when the wave-particle resonant condition is satisfied. With the application of ECCD, the fast electron behavior is observed [25] by the FEB diagnostic, which consists of 9 chords. Figure 5 displays a typical ECCD discharge with the generation of fast electrons. With the ECW injection at 0.25 s, the line integrated FEB intensity signal (I_{FEB}) begins to rise at the central chord (figure 5(*c*)). The electron cyclotron emission (ECE) signal at 80.5 GHz has a resonance layer outside the plasma (+31.96 cm). Its amplitude increases significantly during the ECCD phase, as shown by the black line in figure 5(*e*), and it is dominated by relativistically downshifted emission of fast electrons. The suprathermal electrons are observed during ECCD in many other devices, e.g. in TCV [26, 27], and its impact on the ECE measurement in T-10 [28]. Based on these works, further investigation on the suprathermal electrons will be conducted in the future. As shown in figure 5(*g*), I_{FEB} increases significantly at all energies after applying ECCD. Fast electrons with energy of 30–250 keV are generated when ECCD is applied. The radial profile of I_{FEB} can be obtained by combining the detector signals of different positions and by using an Able-inversion method to derive

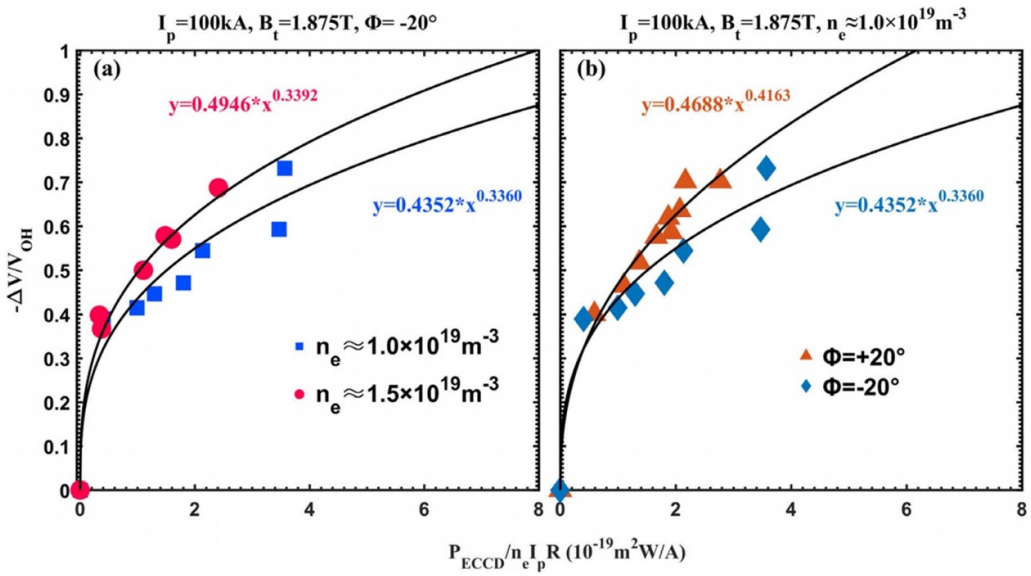

Figure 4. Experimental dependences of $-\Delta V/V_{\rm OH}$ on the normalized ECW power with (*a*) different $n_{\rm e}$ and (*b*) different ECCD toroidal angle, Φ. The fitting (curves) gives (*a*) $n_{\rm e} = 1.0 \times 10^{19}$ m^{-3}: $\eta_0 = (0.080 \pm 0.017) \times 10^{19}$ A m^{-2} W^{-1}; $n_{\rm e} = 1.5 \times 10^{19}$ m^{-3}: $\eta_0 = (0.125 \pm 0.003) \times 10^{19}$ A m^{-2} W^{-1}. (*b*) $\Phi = +20°$: $\eta_0 = (0.160 \pm 0.005) \times 10^{19}$ A m^{-2} W^{-1}. Reproduced from [22].

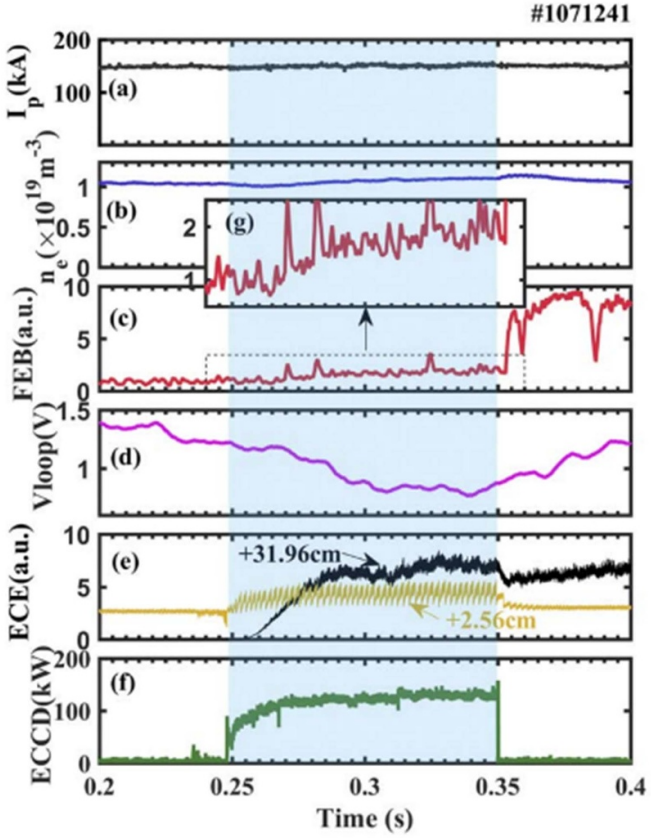

Figure 5. Temporal evolution of typical on-axis ECCD discharges with the generation of a large number of fast electrons. (*a*) The plasma current (*b*) $n_{\rm e0}$ (*c*) FEB signal at the plasma core (*d*) the loop voltage, (*e*) ECE signals with the resonance layers at +2.56 cm (yellow) and +31.96 cm (black) (*f*) $P_{\rm ECCD}$. (*g*) The enlarged FEB signal of dashed box. Reproduced from [25].

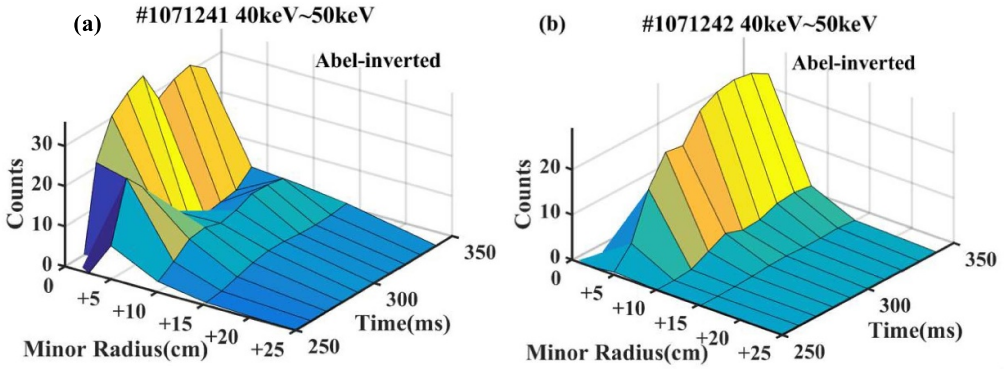

Figure 6. Radial profiles of FEB emissivity derived from Abel-inversion for ECCD (*a*) on-axis and (*b*) off-axis. Reproduced from [25].

the localized emissivity. Figure 6 displays the inverted radial profile of I_{FEB} for ECCD deposited either on-axis or off-axis, and both radial profiles of FEB emissivity display the maximums near the corresponding deposition locations. This can be used to determine the specific deposition area of ECRH in the experiments.

3. Progress on MHD research

The coupling and growth of multiple MHD modes usually lead to significant confinement loss and even major disruption [29, 30]. Hence, extensive studies are carried out on the coupled modes and their impacts on rotation profiles [31], temperature perturbations [32], etc. Recently, the J-TEXT experiments on MHD instabilities pay more attentions on the mode coupling, especially the interaction between 3/1 and 2/1 modes and the control of these modes, as summarized in the following subsections.

3.1. Observations of coupled modes

In J-TEXT, the mode coupling between 2/1 and 3/1 modes often occurs when the edge safety factor, q_{a}, decreases to around 3 [33]. The 2/1 mode is generally a classical TM, while the 3/1 mode can either be a classical TM or an external kink mode (EKM). Figure 7 displays a typical discharge with mode coupling. The power spectrum of the Mirnov signal in the low field side (LFS) midplane (figure 7(*c*)) reveals that 2/1 small magnetic oscillations (SMOs) [34, 35] and 3/1 modes with different frequencies exist simultaneously since 0.3 s. The frequencies of two modes change from different to the same when the coupling between 2/1 SMO and 3/1 mode occurs. Detailed analysis of the spectrum indicates that there are electromagnetic torques between the 2/1 and 3/1 modes, which lead to their final locking at around 0.4 s. After 0.406 s, the phase difference between coupled modes is toroidally in-phase in the LFS midplane (figure 7(*d*)), which leads mutual destabilization of the 2/1 and 3/1 modes and eventually leads to the major disruption (figure 7(*e*>)). Occasionally with the application of ECRH, the phase difference between coupled modes can be observed to be opposite in

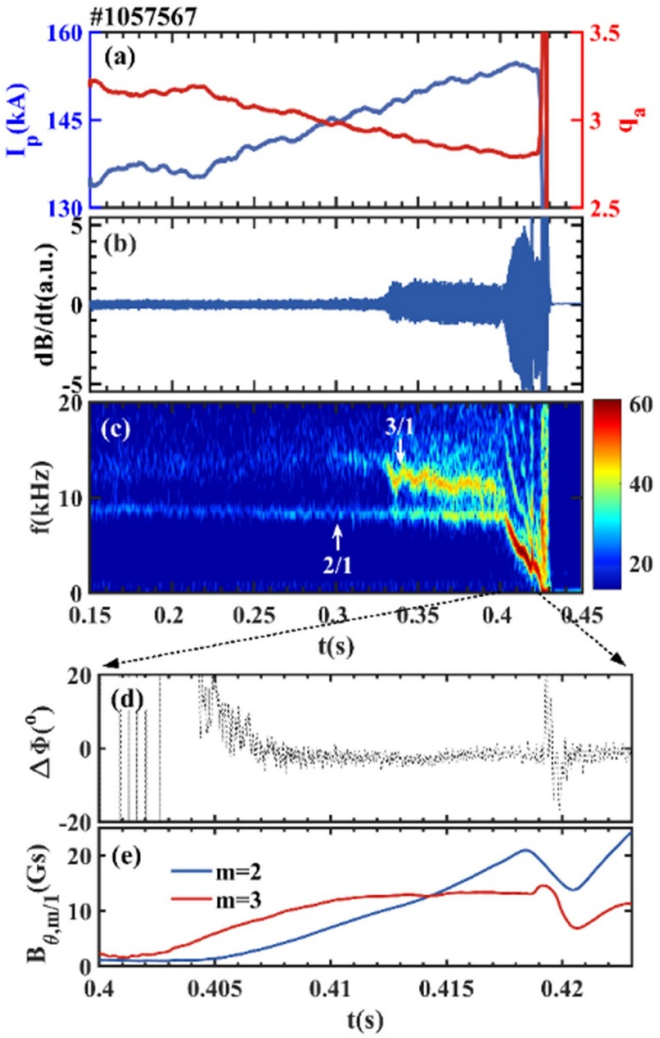

Figure 7. Temporal evolutions of (*a*) the edge safety factor q_{a} (red) and plasma current I_{P} (blue), (*b*) the Mirnov coil signal dB/dt, (*c*) power spectrum of dB/dt, (*d*) the phase difference between 2/1 and 3/1 modes, (*e*) the amplitudes of 2/1 and 3/1 modes. Reproduced from [33].

LFS midplane, as indicated by the slightly stronger MPs measured on the high field side (HFS) midplane than that on the LFS midplane [36].

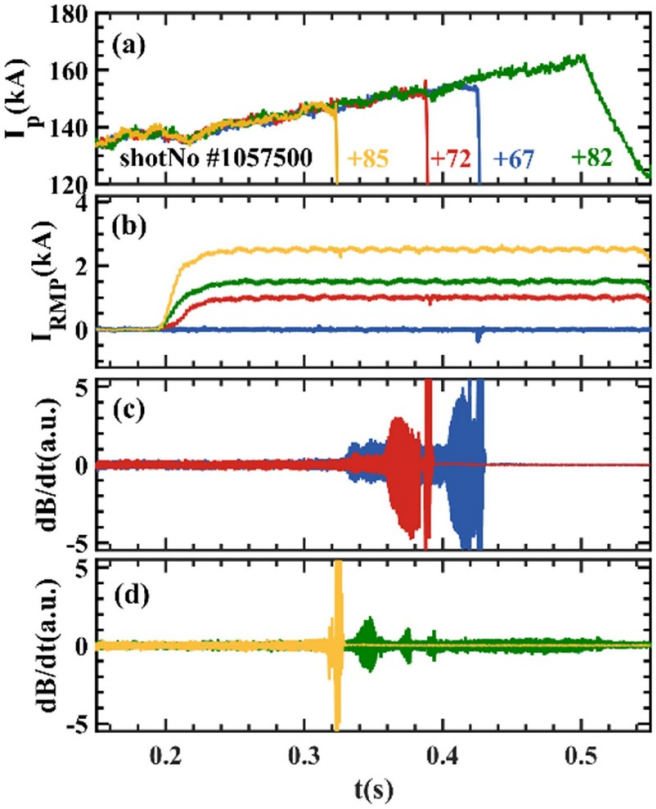

Figure 8. Influence of mixed RMPs with various amplitudes on the disruption due to coupled modes. Temporal evolution of (*a*) I_p, (*b*) the RMP coil current I_{RMP}, (*c*) and (*d*) the Mirnov signals dB/dt. Reproduced from [33]. © IOP Publishing Ltd. All rights reserved.

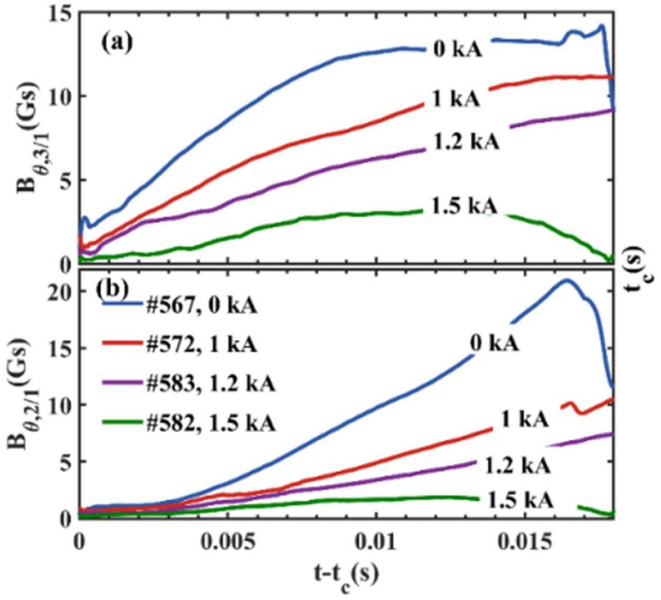

Figure 9. The effect of mixed RMPs with various amplitudes on the evolution of the (*a*) 3/1 and (*b*) 2/1 modes' amplitudes. Reproduced from [33]. © IOP Publishing Ltd. All rights reserved.

3.2. Control of coupled modes and disruption avoidance

Since the coupled MHD modes are dangerous, it is necessary to control them and hence to avoid the major disruption. In the FTU tokamak, by depositing the ECRH power close to one of the RSs, the corresponding mode can be stabilized and then the evolution of the other mode is inhibited [37]. Resonant MPs (RMPs) are capable of suppressing the SMO [34, 35] and the saturated TM with high frequency [38]. Hence, there is a potential of RMP for controlling the coupled modes, which is worth exploring and has been studied in recent J-TEXT experiments.

Figure 8 displays a typical demonstration that the coupled modes can be successfully suppressed during their growth with moderate amplitude of the mixed RMPs [33], which consists of both 2/1 and 3/1 RMP components with comparable amplitudes. By suppressing the growth of coupled modes, the disruption avoidance is achieved, as shown in #1057582 in figure 8. It is considered that the impact of mixed RMP on coupled modes is due to two effects. (a) The mixed RMP can suppress either 2/1 or 3/1 modes which has a high frequency, as shown in figures 9(*a*) and (*b*); (b) the mixed RMP promote the mode coupling between 2/1 and 3/1 modes because of 3/1 RMP component decelerating the 3/1 mode. The competition leads to either the growth or the suppression of the coupled modes. With moderate amplitude, the mixed RMPs suppress the growth of coupled modes and avoid disruption.

Considering the complexity of mixed RMP on mode coupling, two control strategies for preventing mode coupling are proposed and demonstrated by controlling one of the modes using pure 2/1 RMP or 3/1 RMP [39], as summarized in figure 10. It is shown that the 2/1 RMP can prevent the mode coupling by suppressing the 2/1 SMO (#1081903 in figure 10). Moreover, the pure 3/1 RMP with a large amplitude can excite 3/1 locked mode at 0 kHz, while the 2/1 SMO are left with its frequency at around 8 kHz. The excitation of 3/1 locked mode is identified by the growth of $n = 1$ radial magnetic field (green line, figure 10(*b*)) and the appearance of 30 kHz m-BAE modes (figure 10(*e*)) [40]. The frequency difference between 2/1 and 3/1 mode is increased, which prevents the coupling between 2/1 and 3/1 modes (#1080639 in figure 10). These two strategies can break the frequency matching condition between 2/1 and 3/1 modes, and hence avoid mode coupling. With these control strategies, the locking of coupled modes and major disruption are avoided.

3.3. Role of multiple modes on the RMP penetration

Mode coupling effect on the penetration of external RMP field is important, and previous studies focus mainly on the linear effects [41, 42], i.e. no large MHD modes are excited. However, actively driven magnetic island (MI) by RMP might be beneficial for the control of Sawtooth [43] or ELMs [44], and these islands in their nonlinear phase might influence the penetration threshold at other RSs. Recently, such influences attract more and more attentions, especially from modeling via TM1 [45] and MARS-Q [46]. Previous J-TEXT study on the penetration of 3/1 RMP reveals the easy appearance of 2/1

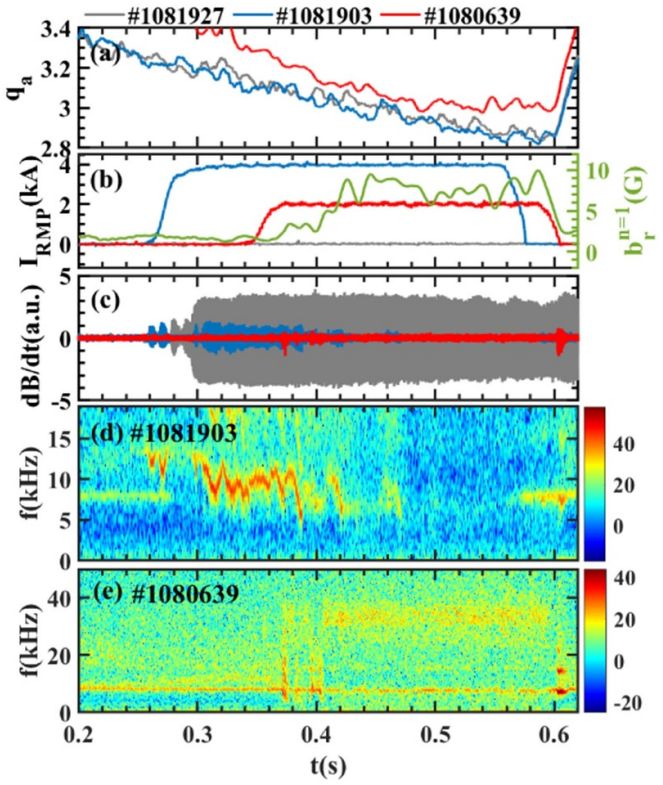

Figure 10. Prevention of mode coupling by either 2/1 RMP (#1081903) or 3/1 RMP (#1080639). Temporal evolutions of (*a*) q_a, (*b*) I_{RMP} (left *y*-axis) and measured $n = 1$ radial magnetic field in #1080639 (right *y*-axis), (*c*) d*B*/d*t*, (*d*) and (*e*) power spectrum of the Mirnov signal showing the mode frequencies and strengths for discharges #1081903 and #1080639, respectively. It is noted that the RMP coils produce pure 2/1 RMP or 3/1 RMP in discharges #1081903 and #1080639 respectively. Reproduced from [39].

locked island after the formation of 3/1 locked island at low density [47], while the applied vacuum 2/1 RMP field is quite small. This might be due to the impact of pre-excited island on the excitation of latter island.

To further investigate this phenomenon, the penetrations of RMP fields with various poloidal spectrum [48] are carried out by scanning the phase difference between the upper and lower coil rows ($\Delta\phi = \phi_{top} - \phi_{bottom}$) and hence changing the ratio between 2/1 and 3/1 RMP components at the corresponding RSs. Here, ϕ_{top} and ϕ_{bottom} are the toroidal phases of $n = 1$ field of each coil rows. It is found that with dominant 2/1 RMP and small 3/1 RMP (or dominant 3/1 RMP and small 2/1 RMP), the penetration of the dominant RMP is observed first, and the penetration thresholds measured by the corresponding resonant component are close for various $\Delta\phi$. By setting $\Delta\phi$ at around 270°, the 2/1 RMP and 3/1 RMP are 0.77 and 1.17 G kA^{-1} at the corresponding RSs, i.e. both RMPs are large. In this case, the successive penetrations of 3/1 RMP followed by the 2/1 RMP is observed. As shown in figure 11(*a*), the 2/1 penetration threshold with a pre-excited 3/1 locked island (diamonds, $\Delta\phi = 270°$) is significantly smaller than the case without 3/1 locked island (squares, $\Delta\phi = 0°$). With the formation of 3/1 locked island, the rotation profile is changed and contributes partially but not completely to the reduction of the 2/1 threshold.

The 3/1 island can produce additional 2/1 MP via toroidal coupling and hence contribute to the total 2/1 field at 2/1 RS. To further study the magnetic contribution of 3/1 mode, the penetration of rotating RMP field is achieved with a special scenario, i.e. with q_a slightly smaller than 3. The penetration of rotating RMP induces 3/1 and 2/1 modes successively [49]. Both modes rotate at the frequency of rotating RMP, i.e. 5 kHz or 4 kHz, and hence the modes' amplitudes can be measured easily by Mirnov probes compared to the 3/1 and 2/1 static islands. The q_a being slightly smaller than 3 allows the 3/1 EKM being easily excited by the rotating 3/1 field even with a small amplitude of 3/1 field. As an important feature of EKM, the amplitude of 3/1 EKM is larger with q_a being closer to 3, as demonstrated by the experimental results with $q_a = 2.78$ (red/blue lines) and 2.67 (green line) in figure 11(*b*). Hence the magnetic contribution from 3/1 mode to the 2/1 RS is easily changed with fixed poloidal spectrum of rotating RMP field, while the modification of the rotation at 2/1 RS by 3/1 EKM would be much smaller than that by 3/1 locked island. This means that the 2/1 RMP produced by 3/1 EKM should have a dominant contribution over the rotation effect, concerning the threshold variation of external RMP field. The large dots (5 kHz) and squares (4 kHz) with error-bars in figure 11(*b*) represent the amplitudes of 3/1 EKM and I_{RMP} at the time of 2/1 field penetration. It is found clearly that the presence of the 3/1 EKM leads to the reduction of the external RMP current required for the 2/1 mode excitation and that the larger 3/1 EKM amplitude can lead to a greater reduction [49].

The penetration of rotating RMP also shows some new features, i.e. the excited 2/1 mode converses from a kink dominant structure to a TM in 5–30 ms [49], which resembles to the conversion during NTM seeding by sawtooth crashes in ASDEX Upgrade [50, 51]. The fast growth of 3/1 EKM might increase the ramping up rate of the total 2/1 RMP field to a sufficient value to induce such conversion, as predicted by numerical modeling [52]. This mode coupling effect may provide a new method to study the forced magnetic reconnection.

4. Disruption prediction and control

The disruption during plasma discharge would result in large thermal loading and electromagnetic force on the surrounding structures and generates REs which can burn holes through structures [14]. The prediction and control of disruption are essential to the safe operation of ITER [14]. The recent J-TEXT efforts on these topics are summarized in the following subsections.

4.1. Disruption prediction

Recent J-TEXT efforts on the disruption prediction focus on the cross tokamak application of machine learning disruption prediction models with various approaches [53]. The main problem of cross tokamak disruption prediction is the lack of data from the target machine. Previous research achieved

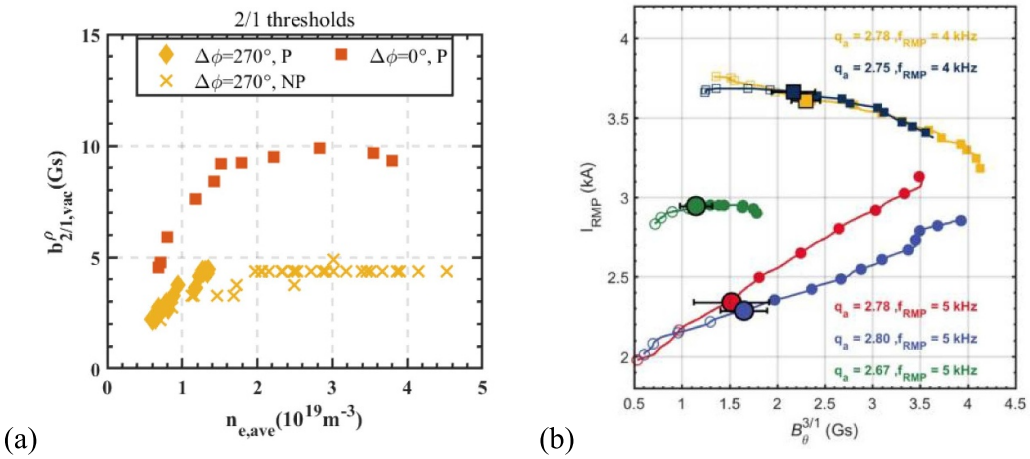

Figure 11. The impact of a pre-excited 3/1 (*a*) locked island or (b) EKM on the excitation of 2/1 island. (*a*) Density dependence of 2/1 external RMP threshold for case with (diamonds) and without (squares) 3/1 locked island. Reproduced from [48]. © 2022 Hefei Institutes of Physical Science, Chinese Academy of Sciences and IOP Publishing. (*b*) The 2/1 mode excitation threshold in ($B_\theta{}^{3/1}$, $I_{\rm RMP}$) space. Reproduced from [49]. © IOP Publishing Ltd. All rights reserved.

cross-tokamak disruption prediction from DIII-D to JET by mixing a small amount of JET's data into the training set [54]. Similarly, predictions are made from DIII-D and C-Mod to EAST by mixing a small amount of disruption data with a large quantity of non-disruption data from EAST [55]. It is observed that differences between the tokamaks may lead to varying levels of difficulty in cross-tokamak disruption prediction. However, the gap between future tokamak reactors and existing tokamak today is substantial [56]. So far, cross-tokamak disruption prediction has only employed the strategy of transfer learning by mixing limited data. This approach may potentially overlook valuable information from the target tokamak due to the limited data available and the substantial differences between tokamaks. We select J-TEXT and EAST to simulate the large gap of tokamaks and attempt superior transfer learning strategies compared to mixed data to tackle this problem from several different perspectives.

First, we adopt the idea that if we can find a feature space in which multiple tokamaks are aligned, then we can make the existing model work on future target tokamak. Although the exact disruption precursor cannot be described, studies show some measurable behaviors are highly correlated with disruption, like the rotating mode slowing down or locked mode and the changes of radiation profile [57]. Guided by those physical hints, we design a manual feature engineering method that extracts normalized features that work across multiple tokamaks. With this physics guided feature extraction method, we achieve great performance on the J-TEXT tokamak (true positive rate (TPR) = 97.27%, false positive rate (FPR) = 5.45%, area under the ROC curve (AUC) = 0.98) [58]. Moreover, those extracted features reduce the divergence between tokamaks. This allows us to develop a novel technique called supervised correlation alignment, which aligns J-TEXT features to EAST's with only a handful of EAST data. The disruption model trained with aligned J-TEXT features gets AUC = 0.833 on EAST test data. This is a huge leap over using J-TEXT trained model on EAST directly which only gets AUC = 0.642 [59].

Recently the development of deep learning solves many hard problems in the scientific community. So, instead of manual feature engineering, we design a deep neural network to extract disruption precursor features. The design of the neural network is also guided by known disruption precursor patterns and principal diagnostics. With this feature extractor, a model is trained on J-TEXT. The bottom layers of the feature extractor are regarded to extract disruption precursor patterns that are common across multiple tokamaks. With those layers frozen, the upper layers are fine-tuned with only 20 EAST discharges to transfer the model to EAST. The transferred model is tested on EAST and gets AUC = 0.811 which is also a huge leap over using J-TEXT trained model on EAST directly which gets AUC = 0.611 [60].

4.2. Disruption mitigation

The understanding of generation and suppression of runaway electrons (REs) is the key issue for large scale devices. A lot of researches on REs are carried out on J-TEXT, including the suppression and dissipation of REs by the MGI (massive gas injection) and RMPs. In recent years, several new tools, such as edge biasing, shattered pellet injection (SPI), are applied on J-TEXT to control REs and disruption. The edge biasing via electrode or limiter can effectively suppress the runaway current, with higher biasing voltage leading to smaller RE current and even completely suppression [61]. During a fast shutdown phase, the Ar SPI has deeper deposition and higher electron density [62] compared to the Ar MGI. The preliminary experimental results of runaway current dissipation based on SPI show that the high Z impurity like argon and neon has a successful dissipation of the runaway current by increasing the thermal radiation. Besides, as the increase of pellet velocity, the impurity assimilation rate would be improved, which

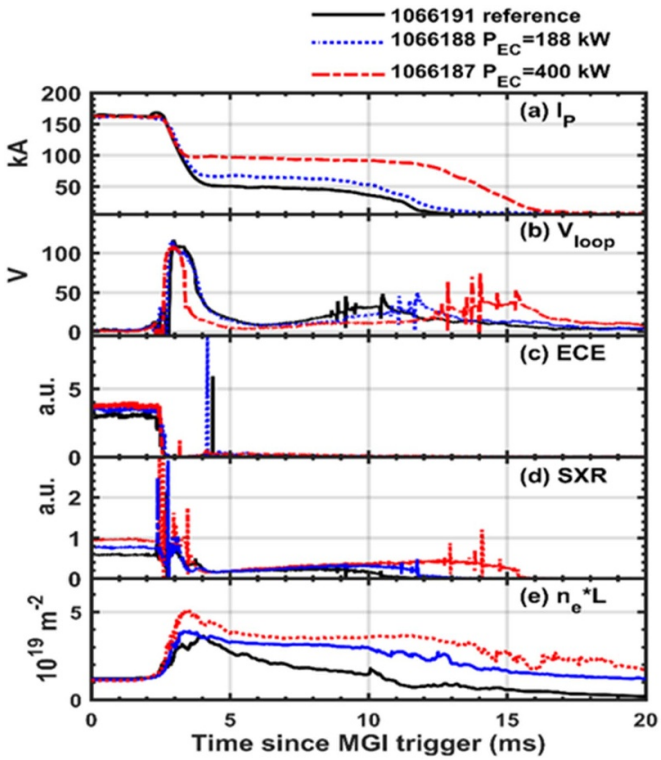

Figure 12. A comparison of time scales and signals of runaway current discharges with and without ECRH. Reproduced from [63]. © IOP Publishing Ltd. All rights reserved.

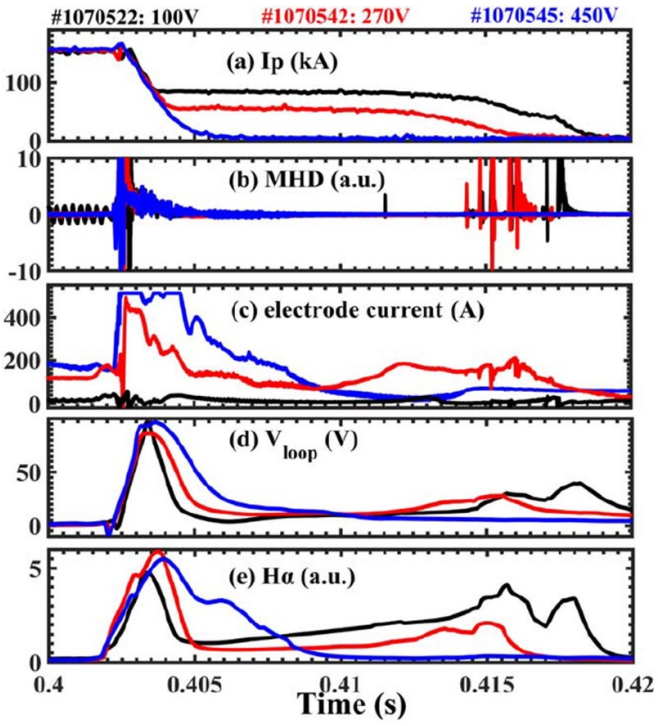

Figure 13. Impact of electrode biasing on the disruption trigged by MGI. The electrode is biased to +100, +270 and +450 V, respectively. Reproduced from [61]. © 2022 Hefei Institutes of Physical Science, Chinese Academy of Sciences and IOP Publishing.

eventually leads to better dissipation efficiency. Especially in J-TEXT, when the pellet is accelerated to about 300 m s^{-1}, the Ar SPI would have a similar effect of runway current dissipation than Ar MGI. Some recent progresses are summarized in detail as follows.

4.2.1. The effect of ECRH on runaway current. During the disruptions triggered by MGI in the ECRH plasmas, the elevation of runaway current are investigated on J-TEXT [63]. The conversion efficiency of runaway current is found to increase from 35% to 75% owing to the suprathermal population when P_{ECRH} is 400 kW, as shown in figure 12. In this experiment, the thermal quench duration decreases from 0.24 ms to 0.11 ms, and the Absolute Extreme Ultraviolet Spectrometer (AXUV) radiative power and n_{e} are about two times higher than the cases without ECRH.

4.2.2. The effect of biasing on runaway current. The suppression of runaway current is also investigated by electrode biasing (EB) and limiter biasing (LB) on J-TEXT [61], which might contribute to an alternative solution for the RE suppression. The typical results are shown in figure 13. The runaway current is found to decrease with the increase of biasing voltage via either EB or LB during both experiments. Moreover, the runaway current is completely suppressed with $U_{\mathrm{EB}} = +450$ V or $U_{\mathrm{LB}} = +300$ V. During the runaway plateau phase, the energy spectra of the REs reveal that the number of REs decreases if the LB with $U_{\mathrm{LB}} = +200$ V is applied. Significant decreases are observed in both the REs' radiation temperature T_{HXR} and the maximum energy (E_{RE}). These indicate that both the number and energy of the REs are reduced, and that the reduction of the runaway seeds leads to the suppression of runaway current. The electric field generated by the biased voltage may be the key factor to suppress the runaway current, and the radial electric field is measured to increase obviously if the biasing voltage is applied. This may lead to an increase in the REs loss and hence to the suppression of runaway current.

4.2.3. Development of electromagnetic pellet injector for disruption mitigation. Currently, actively injecting a large number of particles is the key strategy for disruption mitigation. Such injection is generally achieved by high pressure gas, and its injection speed is limited by the sound speed of the propellant gas. The electromagnetic pellet injection (EMPI) system is a novel high-speed injection system for injecting massive material, and it can provide rapid and effective disruption mitigation. The effective improvement of its injection speed and the reduction of its response time are obtained by using electromagnetic force to launch pellets, which overcomes the limitations of other systems [64, 65].

EMPI configuration is formed by reverse concatenating two railguns, as shown in figure 14 for a schematic diagram. Compared to a conventional railgun system, a deceleration

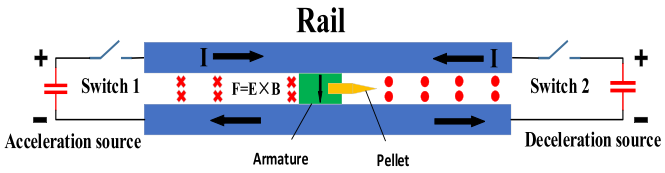

Figure 14. EMPI configuration.

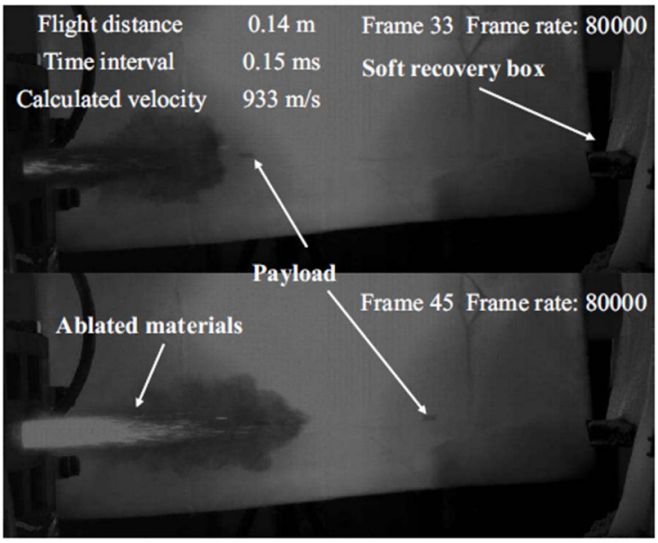

Figure 15. Separated payload flying out of the muzzle. Reproduced from [64]. © 2023 Chinese Physical Society and IOP Publishing Ltd.

railgun barrel is formed by applying an additional pulse power supply at the muzzle of the railgun. Based on the EMPI concept, the payload can be accelerated to above 1000 m s^{-1} and the overall reaction time can be shortened to a few milliseconds. A prototype injector, EMPI-1, is designed and assembled, so as to verify the injection ability and to test its stability. As shown in figure 15, the preliminary test is carried out by using a 5.9 g armature to propel a dummy pellet. Pellet in-bore release test is also conducted successfully and achieves a maximum pellet velocity of 900 m s^{-1} with decelerating the armature velocity to below 200 m s^{-1}. The trajectory of the pellet after separation is also traced along the injection axis. These results suggest that the EMPI configuration has a great potential to be the disruption mitigation system of the large-scale fusion devices.

5. Progress of the study on high-density disruptions

Stable operation at high density is of great interest for fusion reactors. However, constraints on the maximum attainable density are imposed by the density limit during current-generation tokamak operations. The tokamak density limit is generally considered to be associated with progressive cooling of the plasma edge [66], which is found to be closely related to particle confinement degradation [67–70]. Recent J-TEXT experiments emphasize the role of edge physics on high density operation. Several aspects have been studied, and they are summarized as follows.

5.1. Spontaneous and externally driven shear flow evolution near the density limit

As the density approaches Greenwald density n_G on J-TEXT, the edge shear flow and turbulent particle transport events is experimentally studied. Reduced edge shear flow and enhanced particle transport are observed. The results of kinetic and internal energy evolution indicate that shear layer collapse triggers turbulent transport events [71]. A higher density before disruption can be realized by maintaining the edge shear layer via an external biased electrode [72].

As n_e approaches n_G, edge $E \times B$ shear flow and electron temperature decreases, as shown by figures 16(*a*) and (*b*). The radial electric field E_r is obtained from the negative radial gradient of plasma potential ϕ_p, which is measured by a Langmuir probe array [71]. Thus, the $\boldsymbol{E}\times\boldsymbol{B}$ shear flow is calculated as $v_{\theta,E\times B} = \nabla_r\phi_p/B_t$. According to the radial force balance relation which determines E_r, i.e. $E_r = \nabla_r P_i/(Z_i e n_i) - v_{\theta i}B_\phi + v_{\phi i}B_\theta$, the experimental E_r contains the contribution of the diamagnetic term, the poloidal rotation term and the toroidal rotation term. The energy transfer strength from turbulence to zonal flow, which is characterized by the dimensionless ratio of Reynolds power to production power (i.e. P_k/P_I) decreases, while the relative turbulence spreading power (i.e. P_S/P_I) increases significantly, as shown by figures 16(*c*) and (*d*). This suggests that shear layer collapse triggers turbulence spreading events, e.g. blobs. Instead of driving the turbulent Reynolds power, fluctuation power is channeled to turbulence spreading. It is also found that adiabaticity $\alpha = k_\parallel^2 v_{th,e}^2/\nu_{ei}\omega$ passing from adiabatic ($\alpha > 1$) to hydrodynamic ($\alpha < 1$) emerges as a key characteristic to signal the onset of enhanced particle transport events in high density discharges,

$$\frac{\mathcal{P}_K}{\mathcal{P}_I} = \frac{\tilde{v}_r\tilde{v}_\theta\partial_r v_\theta}{-c_s^2\tilde{v}_r\tilde{n}\partial_r\langle n\rangle/\langle n\rangle^2} \tag{1}$$

$$\frac{\mathcal{P}_S}{\mathcal{P}_I} = \frac{-\partial_r\tilde{v}_r\tilde{n}^2c_s^2/2n^2}{-\tilde{v}_r\tilde{n}c_s^2\partial_r\langle n\rangle/n^2} \tag{2}$$

A biased electrode is used to sustain the edge shear layer in high density discharges [72]. A stable increase in line averaged density before disruption is observed along with a strong increase (~2 times) in edge density with 240 V biasing, as shown by figures 17(*a*) and (*b*). Turbulent particle transport and turbulence spreading decrease and electron adiabaticity α increases significantly, as shown by figure 17(*c*). Biasing voltage modulation experiments show that an increase in the edge shear ω_s leads to the increase in adiabaticity in the hysteresis loop of $\omega_s - \alpha$ phase space, as shown by figure 17(*d*).

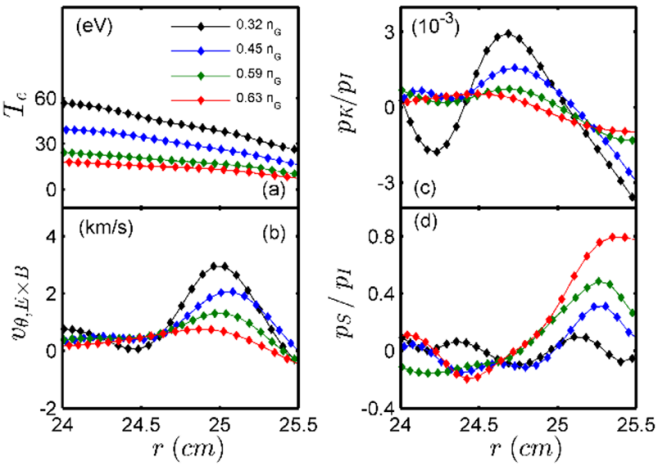

Figure 16. Edge electron temperature, shear flow, kinetic and internal energy evolution as density approaches n_G. Reproduced from [71]. © 2021 IAEA, Vienna.

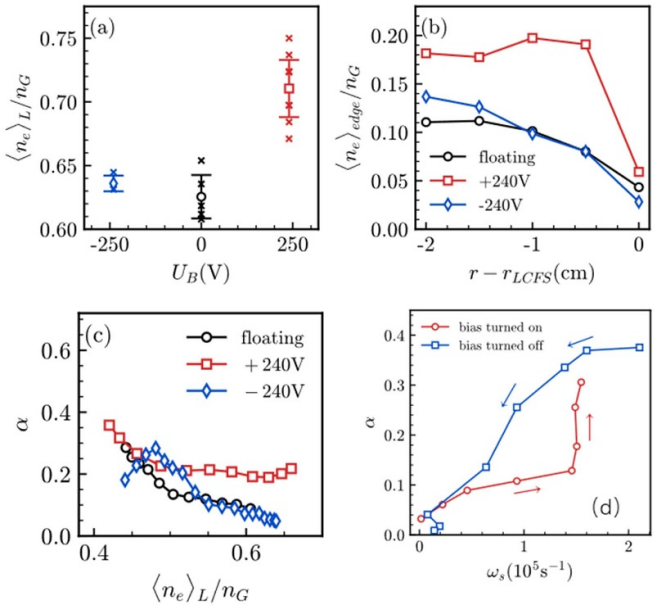

Figure 17. (*a*)–(*b*) The maximum attainable line-averaged and edge density with −240/0/240 V biasing; (*c*) evolution of α; (*d*) hysteresis loop in $\omega_s - \alpha$ phase space. Reproduced from [72]. © 2022 IAEA, Vienna.

These results suggest that external edge $E \times B$ flow shear drive may be of interest for sustaining edge plasma states in high density operation.

5.2. Observation of the high-density front at HFS

High-density front at the HFS is observed on J-TEXT by POLARIS as shown in figure 18 [73]. The high-density front forms in the HFS SOL when n_e reaches a critical value and maintains stable as long as n_e remains. With continuously increasing density, the high-density front expands poloidally and even propagates into the main plasma region, and eventually triggers the major disruption. With the increase of I_P, the

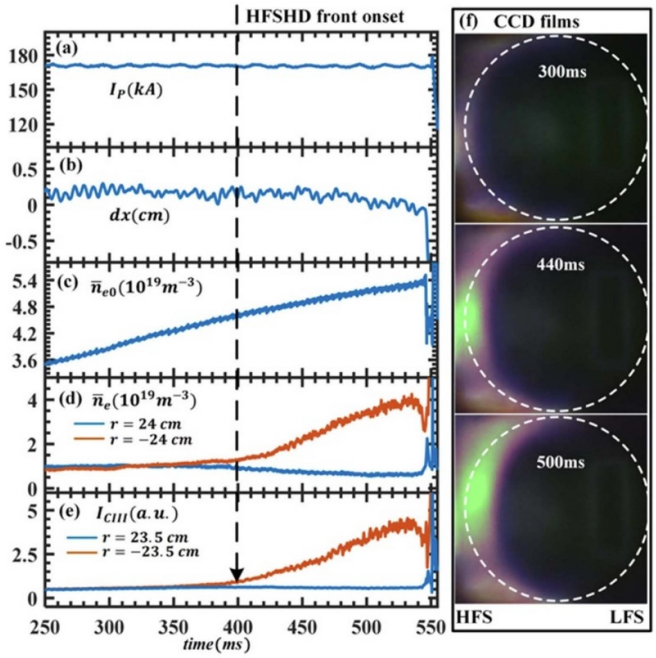

Figure 18. Time evolution of the main parameters for a typical discharge (#39669) of density ramping to limit disruption in J-TEXT. The high-density front occurs at 0.4 s. (*a*) I_p, (*b*) horizontal plasma displacement, (*c*) central line-averaged n_e, (*d*) line-averaged n_e at the most edge of HFS and LFS, (*e*) line emission of CIII, (*f*) visible CCD camera films with the LCFS denoted by the dotted circles. Reproduced from [73]. © IOP Publishing Ltd. All rights reserved.

density threshold for the formation of the high-density front and the maximum density of the region itself increase, sharing similar relationships with density limit on J-TEXT. This indicates that the high-density front might play an important role in setting the maximum achievable density. The high-density front also shares many similarities to MARFE (multifaceted asymmetric radiation from the edge), such as both occurring at the HFS boundaries and exhibiting localized high density. However, there are also obvious differences between them. The radiation power from the region of high-density front is significantly lower than that of MARFE, as illustrated by figure 3 in [73]. And the high-density front is much stable at the inner target or HFS edge across a broad range of plasma density, which is in contrast to the unstable behavior of MARFE. However, the high-density front evolves in its final stage to a MARFE-like behavior. This suggests that MARFE might be the result of these high-density fronts forming in or moving into regions where the plasma temperature and impurity concentration are conducive for them to be radiatively unstable.

5.3. High-density experiment under poloidal divertor configuration

The poloidal divertor configuration discharge is realized in J-TEXT [74]. High-density experiments are attempted to explore the performance of the middle single null (MSN)

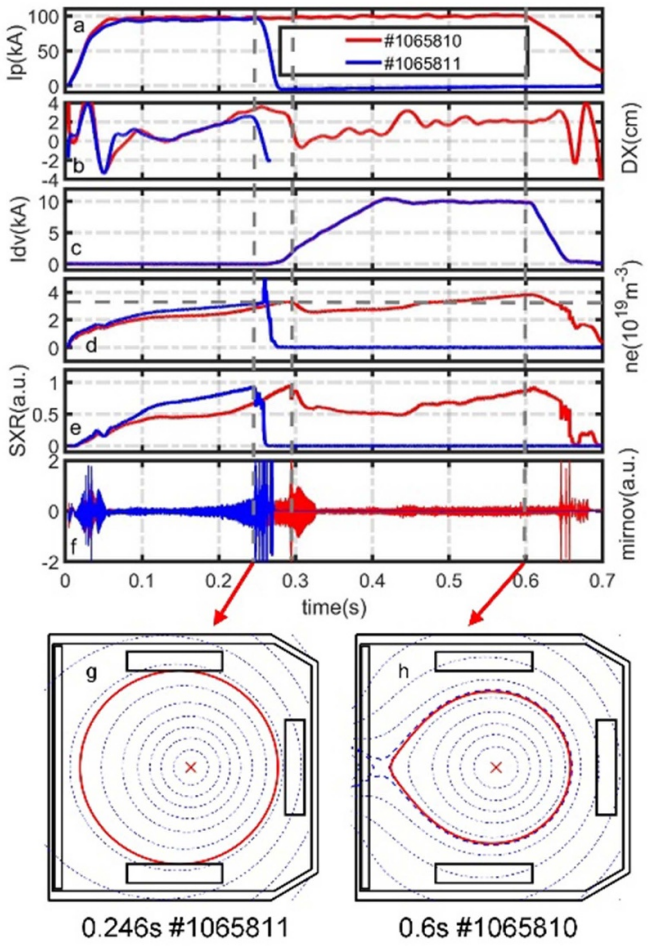

Figure 19. High-density discharges (top) in the limiter configuration (#1065811) and the divertor configuration (#1065810): time evolutions of (*a*) plasma current, (*b*) plasma displacement, (*c*) divertor current I_{dv}, (*d*) line-averaged density at $r_{chord} = 3$ cm, (*e*) central soft x-ray, (*f*) Mirnov signal. Slices of reconstructed flux surface contours of two discharges (*g*) and (*h*). Reproduced from [74]. © 2022 Hefei Institutes of Physical Science, Chinese Academy of Sciences and IOP Publishing.

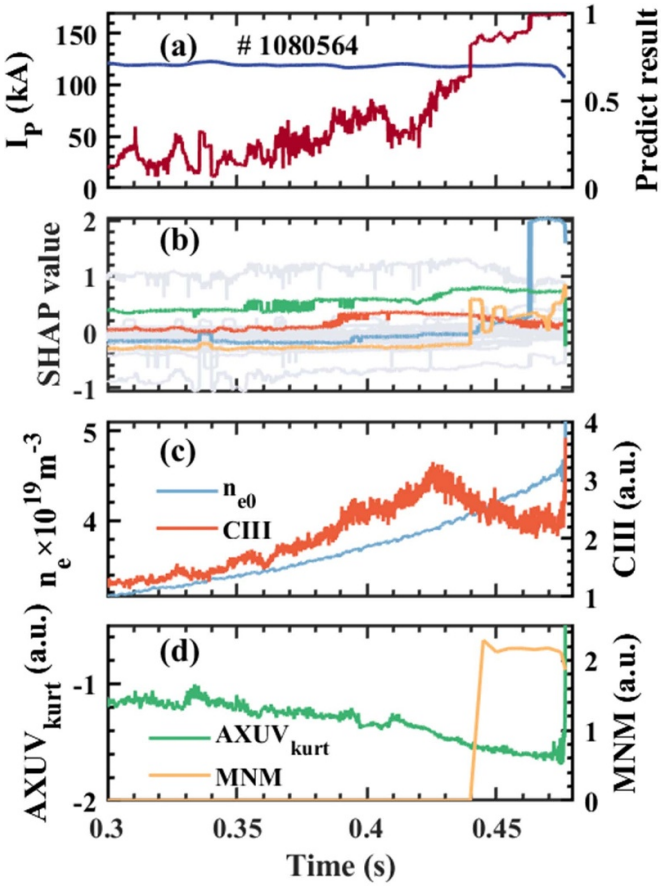

Figure 20. The four typical features along with the predicted result and SHAP value in # 1080564 discharge without RMPs. The navy-blue line represents the plasma current (I_P) and the dark-red line represents the predicted result in (*a*). The light blue lines represent the line average density of the middle channel (n_{e0}) of the SHAP value and feature value in (*b*) and (*c*), respectively; the orange lines represent the impurities radiation (CIII) in in (*b*) and (*c*); the green lines represent the kurtosis of AXUV array ($AXUV_{kurt}$) in (*b*) and (*d*); The yellow lines represent the poloidal mode number (MNM) in (*b*) and (*d*). Reproduced from [58]. © 2023 The Author(s). Published on behalf of IAEA by IOP Publishing Ltd.

divertor configuration. Figure 19 shows a high-density disruption discharge (#1065811) and a high-density discharge (#1065810) with the divertor configuration. In discharge #1065811, the plasma disrupts before the transition to divertor configuration, i.e. still in the limiter configuration at the disruption moment (figure 19(*g*)), and the line-averaged density ($n_{e,ave}$) at $r_{chord} = 3$ cm goes up to around $3.1 \times 10^{19}\,m^{-3}$ at 0.25 s, as shown in figure 19(*d*). It reaches 63.3% of the corresponding Greenwald density $n_G = 4.9 \times 10^{19}\,m^{-3}$. In the divertor configuration discharge #1065810, though there is a minor collapse which happens when $n_{e,ave}$ reaches $3.1 \times 10^{19}\,m^{-3}$, the plasma survives and enters the divertor configuration during the I_{dv} flattop. Then $n_{e,ave}$ increases to a maximum of $3.8 \times 10^{19}\,m^{-3}$ without disruption. Considering that the vertical radius b is smaller in MSN configuration, $n_{e,ave}$ is modified to be $4.9 \times 10^{19} m^{-3}$ taking $b = 0.2$ m. The diverted plasma safely achieves 76.5% of n_G, where $n_G = 6.4 \times 10^{19}\,m^{-3}$ by considering the elongation $\kappa = 0.87$ and the poloidal cross-section area $S = 0.137\,m^2$. It implies that the density limit has not yet been reached. Compared to the limiter configuration, the MSN divertor configuration exhibits to be more stable when the density is near n_G in the experiments.

5.4. Interpretability disruption prediction application on density limit experiment

The interpretable disruption predictor IDP-PGFE [58] in J-TEXT could not only predict disruption but also analyze the disruption causes or event chain. IDP-PGFE is applied to analyze how the RMPs increase the density limit disruption. The discharge without the application of RMP (#1080564) reaches the density limit of about $0.79n_G$. However, the discharges with the application of 2 kA RMPs (#1080550) reach the highest density limit of about $0.91n_G$ in J-TEXT. Figures 20

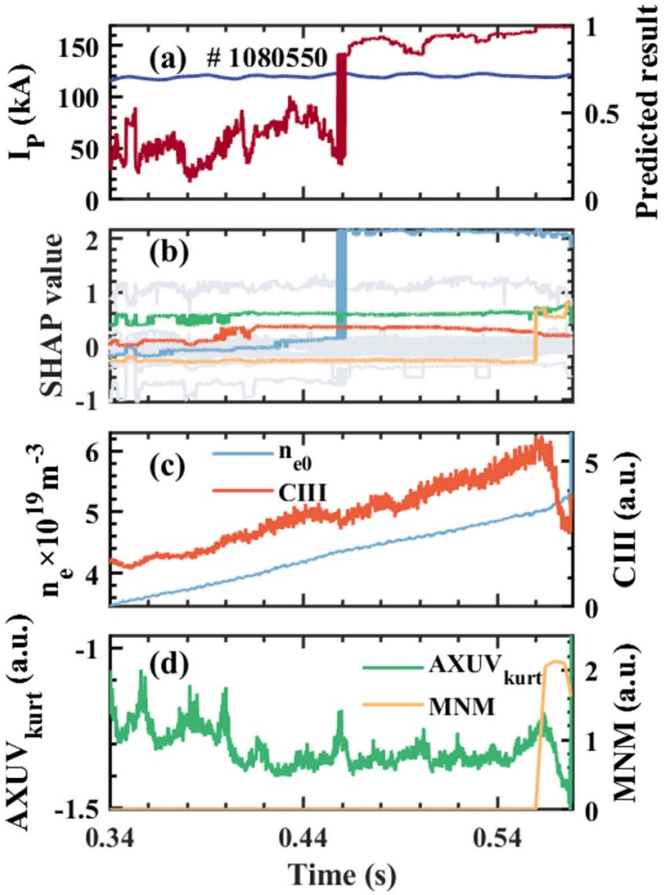

Figure 21. The four typical features along with the predicted result and SHAP value in # 1080550 discharge with RMPs. (*a*)–(*d*) show the same as figure 20. Reproduced from [58]. © 2023 The Author(s). Published on behalf of IAEA by IOP Publishing Ltd.

and 21 show the predicted result, SHAP value and four typical features of these two discharges. Compared to the discharge without the application of RMP (#1080564), the discharges with the application of RMPs (#1080550) raise the density limit by delaying detached plasma and MHD instabilities before the density limit disruption. The application of RMPs decrease the contribution of CIII, $AXUV_{kurt}$ and MNM, makes that even though contribution of the density is already high, the probability of the density limit disruption is still low. This indicates that the application of RMPs not only has an impact on MHD instabilities but also has an impact on the radiation profile. This again shows that the physical mechanism of density limit disruption is not line average density of the middle channel, but is related to radiation and MHD instabilities. The implementation of RMPs establishes a firm link between radiation (profile) and MHD instabilities with disruptions at the density limit. In such disruptions, there's a noticeable increase in the contribution from both radiation (profile) and MHD instabilities prior to the disruption. Therefore, the application of RMPs makes the contribution of radiation (profile) and MHD instabilities rise after

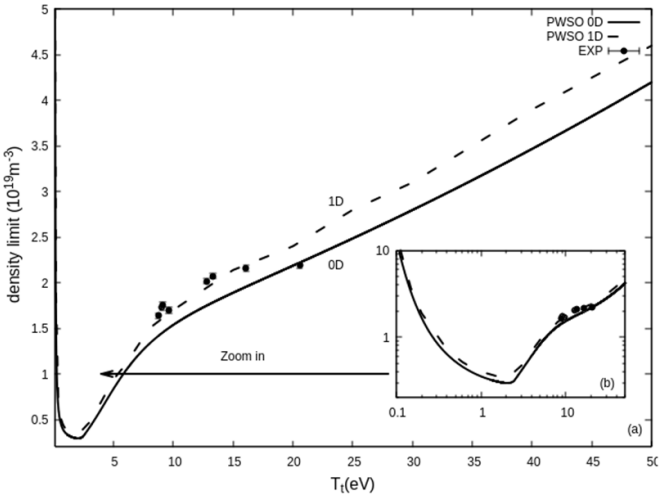

Figure 22. The density limits as functions of the target region plasma temperature T_t using (*a*): linear and (*b*): logarithmic coordinates as predicted from the pwso 0d (solid line) and 1d (dashed line) models in comparison with the experimental data (circular symbol). The experimental data are their averaged values in a time interval [200 ms, 250 ms] of flat-top phase. Reproduced from [76]. © 2023 The Author(s). Published on behalf of IAEA by IOP Publishing Ltd.

the density limit ($\sim 0.79 n_G$), so that the density limit is raised ($\sim 0.91 n_G$).

5.5. Validation of PWSO model for density limit with ECRH

Recently, the Plasma-Wall Self-Organization (PWSO) model [75] was proposed as a potential underlying physics mechanism for the radiative density limit in tokamaks. Impurity radiation is largely controlled by plasma-wall interactions in tokamaks. This radiation affects the amount of heat reaching the limiter/divertor targets, subsequently determining the plasma temperature in the target region. The target region temperature significantly impacts impurity production, which in turn influences impurity radiation. This feedback mechanism forms the foundation of the PWSO model.

This model predicts a significantly enhanced density limit, which may be attainable in tokamaks with ECRH-assisted ohmic startup and sufficiently high initial neutral density. To validate such a density limit scenario based on this model [76], experiments have been conducted on J-TEXT in limiter configuration and ohmic or ECRH assisted Ohmic discharges, with a toroidal magnetic field of 1.875 T and a plasma current of 120 kA. The experimental results demonstrate that increasing the pre-filled gas pressure or ECRH power during the start-up phase can help enhance plasma purity and decrease the CIII radiation level as well as increase the target region plasma temperature. And this generally leads to a higher density limit at the flat-top, as depicted in figures 3 and 4 of [76]. Besides, the PWSO 0D and 1D model are applied to calculate the density limit of J-TEXT. As shown in figure 22, The J-TEXT experimental data quantitatively agree

with the PWSO model's predictions under some parameter assumptions.

6. Turbulence and transport study

6.1. Argon transport studied with XICS

The impurity transport is very important for burning plasma [15]; in particular, highly charged impurities may accumulate in the core and hence lead to the deterioration of plasma performance and even trigger disruption via radiation losses [77]. In the L-mode plasmas, the transport is generally found to be anomalous, even in the plasma core. The impurity accumulation in the core seems to be connected with the change in the sign of the neo-classical convective term and the disappearance of sawtooth oscillations. To study these effects on J-TEXT, light impurities are not suitable since they are fully ionized in the core, and hence argon gas is injected into the J-TEXT plasmas to investigate the core transport of impurity. The helium-like argon ions exist in a very broad range of T_e and reliable results can be achieved for the most important processes of excitation.

The tangential x-ray imaging crystal spectrometer (XICS) [78], designed to measure T_e, ion temperature and plasma rotation velocity on J-TEXT, can be used to study impurity transport of selected impurity [79], such as helium-like argon ions. On J-TEXT, the XICS can receive Ar XVII emissions from $-0.5a$ to $+0.5a$ region at a vertical spatial resolution of 1.8 cm, with a the minor radius. Argon gas is injected at the discharge flattop with an amount of $\sim$1% of fuelling hydrogen gas, so that the injected argon ions do not have significant effect on the discharge. It is shown experimentally that precursor oscillations with a sawtooth appearance are beneficial for the transport of argon ions to the wall. By depositing the ECRH power inside or outside the sawtooth inversion radius ($r_{\rm inv}$), the argon behavior can be significantly modulated. If deposited outside $r_{\rm inv}$, larger precursor oscillations before sawtooth crashes are induced and promote the argon transport. If deposited inside $r_{\rm inv}$, oscillations in the mid-phase of the sawtooth is induced and enhance the argon transport. Analysis shows that these oscillations can result in an outward convection velocity, indicating that the argon ions are transported to the wall. Besides, the mid-phase oscillations enhance the argon transport strongly. The typical results is shown in figure 23, the results of transport parameters is obtained by STRAHL [80].

6.2. Theoretical study on the micro-turbulence and confinement

In addition to the aforementioned experimental study on helium-like argon ions [80], it would be also important to study the effects of helium ions, which include both 3.5 MeV alpha (α) particles and helium ash coming from the slowed down α particles [81]. Currently such study is not possible on J-TEXT, so we proceed the researches by using kinetic theory. By deriving the quasi-neutrality equation with energetic particles (EPs) such as α particles and beam driven fast ions, it is found that increasing the fraction of EPs reduces the linear growth rate of electron temperature gradient ($\nabla T_{\rm e}$) driven collisionless trapped electron mode (CTEM) instability [82]. This is qualitatively consistent with gyrokinetic simulation results [83], and verifies the applicability of our analytical model. Then, we focus on the electron density gradient ($\nabla n_{\rm e}$) driven CTEM instability, which is destabilized by the presence of EPs. This is because the real frequency is further downshifted by the dilution effects of EPs, then more electrons can resonant with drift wave and results in greater growth rate. Different with α particles, the helium ash with its temperature being comparable with the background deuterium–tritium (D–T) ions stabilizes the $\nabla n_{\rm e}$ driven CTEM instability [84, 85]. Comprehensively, for the D–T plasmas with both α particles and helium ash, it is pointed that the destabilization from 3% α particles with its density gradient being twice that of electrons, i.e., $R/L_{{\rm n}\alpha} = 2R/L_{\rm ne}$ is stronger than the stabilization from 10% helium ash with fixed temperature $T_{\rm z} = 10$ keV and the density gradient equaling that of electrons, i.e. $R/L_{\rm nz} = R/L_{\rm ne}$. On the basis of these works, the quasi-linear flux of helium ash is further derived, and it is found that the presence of α particles enhances the efficiency of helium ash removal since the ratio of helium ash diffusivity to the effective electron thermal conductivity i.e. $D_{\rm He}/\chi_{\rm eff}$, is increased by α particles [86]. Besides, by combining the destabilizing effects of α particles on CTEM instability and their role in reduction of total polarization shielding, the generation of zonal flow by CTEM turbulence is enhanced by α particles, and it may indicate better confinement in burning plasmas with EPs [87].

It is shown that the RMP can effectively control the TM and coupled MHD modes in J-TEXT. However, the effects of toroidal symmetry breaking of magnetic configuration induced by RMP or MHD instability on transport and micro-instability are also important. In addition to the effects of RMP on the loss of EPs in tokamak pedestal based on the single particle orbit model [88], the effects of three-dimensional (3D) MP on the confinement of tokamak plasmas are also systematically studied from the viewpoint of both neoclassical and micro-turbulence. The neoclassical toroidal viscosity (NTV) torque caused by the 3D MP generated from the internal kink mode (IKM) and its influence on toroidal rotation are studied. It is proposed that the transition of the intrinsic rotation between the electron root and the ion root determined by NTV theory may be the physical mechanism which causes the experimental observed intrinsic toroidal rotation reversal [89]. Using this newly proposed model, the scaling of threshold density for reversal is further predicted to be proportional to $T_{\rm e0}^{5/2}/B$ based on the transition of collisionality regimes of neoclassical transport, and is also verified by using the NTVTOK code [90] simulation together with the momentum transport analysis [91]. Here, $T_{\rm e0}$ and B represent the core electron temperature and equilibrium magnetic field strength, respectively. To further test this new model, experiments are conducted on J-TEXT. It is observed that the amplitude of IKM increases with the ECRH power, and that the core toroidal

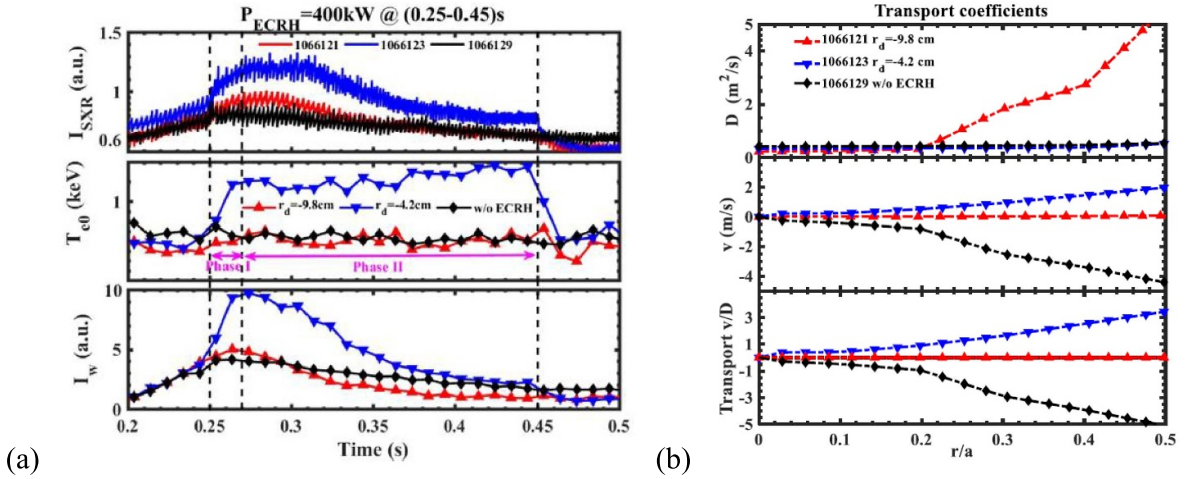

Figure 23. (*a*) Time evolutions of core SXR radiation, core T_e and w line intensity (I_w) of Ar XVII in the core; (*b*) transport parameters obtained by the best reconstruction of the time evolutions of experimental radiation for discharges shown in (*a*). Reproduced from [80].

rotation in counter-current direction is reduced, in particular for low density condition. The corresponding NTVTOK simulation shows that the NTV torque caused by the IKM plays a key role in changing the intrinsic core toroidal rotation, which is qualitatively consistent with the experimental observations [92]. Besides, the effects of 3D MP with different topology configurations on micro-turbulence and anomalous transport are also expounded as follows: (1) for the case with flux surface distorted by the IKM, the synergetic effects of 3D MP with the stabilizing phase and finite beta are helpful to stabilize the CTEM instability, thus are possible to reduce the external power to trigger the internal transport barrier formation [93]; (2) for the case with flux surface changed by magnetic reconnection from the MI, the toroidal ion temperature gradient (ITG) mode inside the MI is stabilized, and the flow shearing rate around the X (O) point boundary of bigger MI is greater (smaller) than the linear growth rate of toroidal ITG, which indicates that the micro-turbulence spreading into the MI is more likely to occur around the O point boundary of bigger MI [94]; for the case with stochastic flux surface caused by the overlap of MI, the non-ambipolar current density generated by stochastic magnetic field can influence the particle, momentum and heat transport, thus further influence the radial electric field and the L–H transition [95].

7. Summary and outlook

Over the last two years, J-TEXT continuously made great efforts on upgrading its auxiliary heating systems and diagnostic systems, so as to increase the plasma parameters and to enhance the capability of measuring and controlling the plasma. A total ECRH power of 1 MW is available on J-TEXT, with the successful commission of the second gyrotron (105 GHz/500 kW/1 s) in the end of 2022. With the injection of ECW, several physics problem are been investigated. The successful plasma startup can be achieved with the ECRH power above 200 kW, and the minimal required toroidal electric field is reduced from 2.5 V m^{-1} (ohmic) to 0.56 V m^{-1} (with ECRH). For toroidal injection, the ECCD efficiency is derived to be approximately $\eta_0 = (0.06–0.16) \times 10^{19}$ A m^{-2} W^{-1}, and the total driven current is estimated to be ~24 kA ($I_p = 100$ kA) with 300 kW ECW power. During the ECCD phase, fast electrons with energy of 30–250 keV are generated as observed via FEB, and the radial profile of FEB emissivity displays a maximum near the deposition location for either on-axis or off-axis ECCD. For perpendicular injection, the successful suppression of TM is achieved with the ECW power deposited close to the RS. Besides, the runaway current during MGI triggered disruption increases with ECRH power, and the conversion efficiency of Ohmic to runaway current increases from 35% to 75% with 400 kW ECW.

The interaction between 3/1 and 2/1 modes and the control of these modes are extensively studied on J-TEXT. The 2/1 mode is generally a TM, while the 3/1 mode can either be a TM or an EKM. The 3/1 mode is coupled to the 2/1 mode with their toroidal phases in the LFS midplane mostly being the same, while occasionally being opposite with ECRH. When they are in phase in LFS, they usually grow to large amplitudes, locks and leads to major disruption. Such mode coupling can be avoided either by suppressing the 2/1 mode via pure 2/1 RMP or by inducing large static 3/1 locked TM via pure 3/1 RMP. When the applied RMP consists of both 2/1 and 3/1 RMP components, the coupled modes can be suppressed during their growth with moderate amplitude of the RMPs. With these control strategies, the locking of coupled modes and major disruption are avoided. The threshold for exciting 2/1 locked TM is studied with a 3/1 mode pre-induced by external RMPs. It is found that the 2/1 threshold is significantly reduced, whether the 3/1 mode is a locked 3/1 TM with q_a being larger than 3 or a 3/1 EKM with q_a being slightly smaller than 3. These observations emphasize the important role of multiple modes

interaction on reducing the penetration threshold of external RMP field.

The prediction and control of disruption are essential to the safe operation of ITER, and they are further investigated on J-TEXT. Recent J-TEXT efforts on the disruption prediction focus on the cross tokamak application of machine learning disruption prediction models with various approaches. The cross tokamak prediction performance is improved for traditional machine models using manual feature engineering guided by physics and domain adaption technique, and for deep learning models with deep transfer learning techniques. Several new tools, such as edge biasing, SPI, are applied on J-TEXT to control disruption. The edge biasing via electrode or limiter can effectively suppress the runaway current, with higher biasing voltage leading to smaller RE current and even completely suppression. A prototype electromagnetic pellet injector is designed and built, and the maximum pellet velocity of 900 m s^{-1} is achieved.

Recent J-TEXT experiments emphasize the role of edge physics on high density operation. As the density approaches Greenwald density n_G on J-TEXT, the collapse of the edge shear layer is observed and suggested to trigger turbulence spreading events, while particle flux is observed to increase. A biased electrode is then applied in such high-density discharges to sustain the edge shear layer, which would otherwise collapse. The particle transport is found to reduce, and thus higher operational density is achieved on J-TEXT. These results support the hypothesis that the collapse of the edge shear layer triggers the onset of the strong transport and turbulence characteristic of the density limit regime. The density limit is also observed to increase by changing the ohmic plasma from the limiter configuration to the poloidal divertor configuration (with a single null in the HFS midplane).

In the following two years, experimental efforts on J-TEXT will focus on the optimization of ECW and 3D plasma configurations. With 1 MW ECW injected, the plasma parameter will be improved further and perhaps transport barrier either internal or edge might be induced. A new divertor concept, i.e. island divertor configuration, is applied with either an edge 3/1 or 4/1 island on J-TEXT [96, 97]. Future island divertor operation with higher density would provide an important comparison with the limiter and poloidal divertor configurations, on the accessible density and underlining edge physics. Moreover, the interplay among varies 3D plasma configurations (such as, TMs, IKMs, RMP induced islands, island divertor, etc) and the turbulence and transport will be further studied, especially with electron dominant heating.

Acknowledgments

This work is supported by the National MCF Energy R&D Program of China (Contract Nos. 2018YFE0309100, 2018YFE0310300, 2019YFE03010004, 2019YFE03050004, 2022YFE03040004) and the National Natural Science Foundation of China (Nos. 11905078, 12075096, 12047526 and 51821005). ITER is a Nuclear Facility INB-174. The views and opinions expressed herein do not necessarily reflect those of the ITER Organization.

ORCID iDs

Nengchao Wang https://orcid.org/0000-0001-6797-2398
Zhongyong Chen https://orcid.org/0000-0002-8934-0364
Zhoujun Yang https://orcid.org/0000-0002-9141-7869
Zhipeng Chen https://orcid.org/0000-0002-8330-0070
Wei Zheng https://orcid.org/0000-0002-2853-6021
Song Zhou https://orcid.org/0000-0002-1407-0574
Ting Long https://orcid.org/0000-0002-0136-8953
Rui Ke https://orcid.org/0000-0003-0117-0098
Li Gao https://orcid.org/0000-0001-5758-3516
Peng Shi https://orcid.org/0000-0002-1853-0726
Jiaxing Liu https://orcid.org/0000-0002-9641-4368
Weixin Guo https://orcid.org/0000-0001-7677-799X
Lu Wang https://orcid.org/0000-0002-5881-6139
Zhonghe Jiang https://orcid.org/0000-0002-4971-080X
Zhifeng Cheng https://orcid.org/0000-0001-6019-399X
Ping Zhu https://orcid.org/0000-0002-5773-8861
Minghai Liu https://orcid.org/0000-0002-8065-4404
Yong Yang https://orcid.org/0000-0001-7304-7529
Chuan Li https://orcid.org/0000-0003-4761-5160
Ming Zhang https://orcid.org/0000-0002-9372-4926

References

[1] Zhuang G. *et al* 2011 *Nucl. Fusion* **51** 094020
[2] Liang Y. *et al* 2019 *Nucl. Fusion* **59** 112016
[3] Wang N. *et al* 2022 *Nucl. Fusion* **62** 042016
[4] Yang Q. *et al* 2022 *Plasma Sci. Technol.* **24** 054005
[5] TAO Q. *et al* 2022 *Plasma Sci. Technol.* **24** 064011
[6] Li F., Yang Z.J., Gao L. and Fu C.P. 2021 *Rev. Sci. Instrum.* **92** 043503
[7] Wang Y. *et al* 2022 *Plasma Sci. Technol.* **24** 064001
[8] Zhang Z. *et al* 2022 *Fusion Eng. Des.* **177** 113065
[9] Donghui X.I.A. *et al* 2022 *Plasma Sci. Technol.* **24** 124010
[10] Chen X.X. *et al* 2022 The development of 1 MW ECRH system on J-TEXT *Proc. 21st Joint Workshop on Electron Cyclotron Emission (ECE) and Electron Cyclotron Resonance Heating (ECRH) Saint-Paul 2022* (https://doi.org/10.1051/epjconf/202327702004)
[11] Zhang J., Xia D.H., Liu C.H., Wang Z.J. and Pan Y. 2020 *IEEE Trans. Plasma Sci.* **48** 1560
[12] Gormezano C. *et al* 2007 *Nucl. Fusion* **47** S285
[13] Gribov Y., Humphreys D., Kajiwara K., Lazarus E.A., Lister J.B., Ozeki T., Portone A., Shimada M., Sips A.C.C. and Wesley J.C. 2007 *Nucl. Fusion* **47** S385
[14] Hender T.C. *et al* 2007 *Nucl. Fusion* **47** S128
[15] Doyle E.J. *et al* 2007 *Nucl. Fusion* **47** S18
[16] Barabaschi P. 2023 Progress on ITER manufacturing, construction, commissioning and plans *29th IAEA Fusion Energy Conf. (FEC 2023) (16–21 October 2023)*
[17] Lloyd B.T., Jackson G.L., Taylor T.S., Lazarus E.A., Luce T.C. and Prater R. 1991 *Nucl. Fusion* **31** 2031
[18] Kajiwara K., Ikeda Y., Seki M., Moriyama S., Oikawa T., Fujii T. and Team J.-6. 2005 *Nucl. Fusion* **45** 694
[19] De Vries P.C. and Gribov Y. 2019 *Nucl. Fusion* **59** 096043
[20] Zhang J. *et al* 2023 *Nucl. Fusion* **63** 076028
[21] Fang J.G. *et al* 2023 49th *EPS Conf. on Plasma Physics Th_MCF14*

[22] Fang J.G. *et al* 2022 *Plasma Sci. Technol.* **24** 124016
[23] Luce T.C., Lin-Liu Y.R., Harvey R.W., Giruzzi G., Politzer P.A., Rice B.W., Lohr J.M., Petty C.C. and Prater R. 1999 *Phys. Rev. Lett.* **83** 4550
[24] Lloyd B. *et al* 1998 *Plasma Phys. Control. Fusion* **40** A119
[25] Zhang X.B. *et al* 2022 *Plasma Sci. Technol.* **24** 064007
[26] Coda S. *et al* 2003 *Nucl. Fusion* **43** 1361
[27] Choi D., Coda S., Decker J., Cazabonne J.A. and Peysson Y. 2020 *Plasma Phys. Control. Fusion* **62** 115012
[28] Poznyak V.I., Valencia O., Gridina T.V., Piterskii V.V., Ploskirev G.N. and Ploskirev E.G. 2012 *Plasma Phys. Rep.* **38** 679
[29] Wesson J.A. *et al* 1989 *Nucl. Fusion* **29** 641
[30] Suttrop W. *et al* 1997 *Nucl. Fusion* **37** 119
[31] Tobias B. *et al* 2016 *Phys. Plasmas* **23** 056107
[32] Kim G., Yun G.S., Woo M. and Park H.K. 2018 *Plasma Phys. Control. Fusion* **60** 035009
[33] He Y. *et al* 2023 *Plasma Phys. Control. Fusion* **65** 035012
[34] Wang N. *et al* 2014 *Nucl. Fusion* **54** 064014
[35] Wang H.H. *et al* 2018 *Nucl. Fusion* **58** 056024
[36] Ren Z.K. *et al* 2022 48th *EPS Conf. on Plasma Physics* p P4b.126 (available at: https://info.fusion.ciemat.es/OCS/EPS2022PAP/pdf/P4b.126.pdf)
[37] Esposito B., Granucci G., Smeulders P., Nowak S., Martín-Solís J.R. and Gabellieri L. 2008 *Phys. Rev. Lett.* **100** 045006
[38] Jin W., Ding Y.H., Rao B., Hu Q.M., Jin X.S., Wang N.C., Zhang X.Q., Wang Z.J., Chen Z.Y. and Zhuang G. 2013 *Plasma Phys. Control. Fusion* **55** 035010
[39] He Y. *et al* 2023 *Plasma Phys. Control. Fusion* **65** 065011
[40] Liu L. *et al* 2019 *Nucl. Fusion* **59** 126022
[41] Scoville J.T. and Haye R.J.L.A. 2003 *Nucl. Fusion* **43** 250
[42] Park J.-K., Schaffer M.J., La Haye R.J., Scoville T.J. and Menard J.E. 2012 *Nucl. Fusion* **52** 089501
[43] Li J. *et al* 2020 *Nucl. Fusion* **60** 126002
[44] Hu Q., Nazikian R., Grierson B., Logan N., Orlov D., Paz-Soldan C. and Yu Q. 2020 *Phys. Rev. Lett.* **125** 045001
[45] Hu Q., Du X., Yu Q., Logan N.C., Kolemen E., Nazikian R. and Jiang Z.H. 2019 *Nucl. Fusion* **59** 016005
[46] Ye C. *et al* 2023 *Nucl. Fusion* **63** 076004
[47] Hu Q. *et al* 2016 *Nucl. Fusion* **56** 092009
[48] Mao F. *et al* 2022 *Plasma Sci. Technol.* **24** 124002
[49] Zhang Q. *et al* 2023 *Plasma Phys. Control. Fusion* **65** 095017
[50] Igochine V., Gude A., Günter S., Lackner K., Yu Q., Barrera Orte L., Bogomolov A., Classen I., McDermott R.M. and Luhmann N.C. 2014 *Phys. Plasmas* **21** 110702
[51] Igochine V., Gude A., Günter S., Hanson J.M., Lackner K., Paz-Soldan C., Strait E. and Zohm H. 2019 *Nucl. Fusion* **59** 066038
[52] Yu Q., Günter S., Lackner K. and Maraschek M. 2012 *Nucl. Fusion* **52** 063020
[53] Zheng W. *et al* 2023 J-TEXT's recent efforts on machine learning cross tokamak disruption prediction *29th IAEA Fusion Energy Conf. (FEC 2023)* (*London, UK, 16–21 October 2023*) (available at: https://conferences.iaea.org/event/316/contributions/28736/)
[54] Kates-Harbeck J., Svyatkovskiy A. and Tang W. 2019 *Nature* **568** 526
[55] Zhu J.X., Rea C., Montes K., Granetz R.S., Sweeney R. and Tinguely R.A. 2021 *Nucl. Fusion* **61** 049501
[56] Shimada Y. *et al* 2007 *Nucl. Fusion* **47** S1
[57] Rea C., Montes K.J., Pau A., Granetz R.S. and Sauter O. 2020 *Fusion Sci. Technol.* **76** 912
[58] Shen C. *et al* 2023 *Nucl. Fusion* **63** 046024
[59] Shen C. *et al* 2023 49th *EPS Conf. on Plasma Physics* p Th_MCF16
[60] Zheng W. *et al* 2023 *Commun. Phys.* **6** 181
[61] Mou L. *et al* 2022 *Plasma Sci. Technol.* **24** 124001
[62] Li Y. *et al* 2021 *Nucl. Fusion* **61** 126025
[63] Bai R.X. *et al* 2021 *Plasma Phys. Control. Fusion* **63** 115014
[64] Li F. *et al* 2023 *Chin. Phys.* B **32** 075205
[65] Chen Z. *et al* 2022 *Trans. China Electrotech. Soc.* **37** 5056
[66] Greenwald M. *et al* 2014 *Phys. Plasmas* **21** 110501
[67] Singh R. and Diamond P.H. 2021 *Nucl. Fusion* **61** 076009
[68] Hajjar R.J., Diamond P.H. and Malkov M.A. 2018 *Phys. Plasmas* **25** 062306
[69] Hong R., Tynan G.R., Diamond P.H., Nie L., Guo D., Long T., Ke R., Wu Y., Yuan B. and Xu M. 2018 *Nucl. Fusion* **58** 016041
[70] Brower D.L. *et al* 1991 *Phys. Rev. Lett.* **67** 200
[71] Long T. *et al* 2021 *Nucl. Fusion* **61** 126066
[72] Ke R. *et al* 2022 *Nucl. Fusion* **62** 076014
[73] Shi P., Sun H., Zhuang G., Cheng Z., Gao L., Chen Z., Li J., Zhou Y. and Zhou C. 2021 *Plasma Phys. Control. Fusion* **63** 125010
[74] Chen Z. *et al* 2022 *Plasma Sci. Technol.* **24** 124008
[75] Escande D.F., Sattin F. and Zanca P. 2022 *Nucl. Fusion* **62** 026001
[76] Liu J. *et al* 2023 *Nucl. Fusion* **63** 096009
[77] Shimada M. 1992 *Fusion Eng. Des.* **15** 325
[78] Jin W. *et al* 2014 *Rev. Sci. Instrum.* **85** 023509
[79] Yan W., Chen Z.Y., Zhang X.L., Cheng Z.F., Yang Z.J., Shi Y.J., Jin W., Ding Y.H. and Liang Y.F. 2021 *Fusion Eng. Des.* **162** 112084
[80] Yan W. *et al* 2023 *Plasma Phys. Control. Fusion* **65** 055029
[81] Maggi C. *et al* 2023 *Nucl. Fusion* **63** 110201
[82] Hussain M.S., Guo W. and Wang L. 2021 *Plasma Phys. Control. Fusion* **63** 075010
[83] Yang S.M., Angioni C., Hahm T.S., Na D.H. and Na Y.S. 2018 *Phys. Plasmas* **25** 122305
[84] Guo W., Zhang M., Wang L. and Zhuang G. 2021 *Nucl. Fusion* **61** 016020
[85] Guo W. and Zhang M. 2021 *J. Fusion Energy* **40** 8
[86] Zhu G., Wang L., Guo W., Hussain M.S. and Zhang M. 2022 *Nucl. Fusion* **62** 126011
[87] Hussain M.S., Guo W. and Wang L. 2022 *Nucl. Fusion* **62** 056013
[88] Huang H. and Wang L. 2020 *Plasma Sci. Technol.* **22** 105101
[89] Li H., Sun Y., Wang L., He K. and Shaing K.-C. 2021 *Nucl. Fusion* **61** 104002
[90] Sun Y., Li X., He K. and Shaing K.C. 2019 *Phys. Plasmas* **26** 072504
[91] Li H., Sun Y. and Wang L. 2023 *Phys. Plasmas* **30** 052504
[92] Li H. *et al* 2024 Effects of neoclassical toroidal viscosity on toroidal rotation under ECRH on the J-TEXT tokamak To be submitted
[93] Huang Z., Guo W. and Wang L. 2022 *Nucl. Fusion* **62** 066044
[94] Zhang G., Guo W. and Wang L. 2022 *Plasma Phys. Control. Fusion* **64** 045006
[95] Guo W., Jiang M., Diamond P.H., Chen C.-C., Cao M., Li H. and Long T. 2022 *Plasma Phys. Control. Fusion* **64** 124001
[96] Zhou S. *et al* 2023 First application of the island divertor configuration in the J-TEXT tokamak *29th IAEA Fusion Energy Conf. (FEC 2023)* (*London, UK, 16–21 October 2023*) (available at: https://conferences.iaea.org/event/316/contributions/28032/)
[97] Liang Y. *et al* 2022 *Plasma Sci. Technol.* **24** 124021